Piecewise Average-Value Model of PWM Converters With Applications to Large-Signal Transient Simulations

Yin Xu, *Member, IEEE*, Ying Chen, *Member, IEEE*, Chen-Ching Liu, *Fellow, IEEE*, and Haixiang Gao, *Student Member, IEEE*

***Abstract*—State-space average-value models (AVMs) of pulse width modulation converters are widely used in both small-signal frequency-domain analysis and large-signal time-domain transient simulations. This paper is focused on the latter category. The limitations of the traditional state-space AVM (T-AVM) are discussed. A piecewise state-space AVM, P-AVM, is proposed, which uses the actual duty ratio as the control input instead of the continuous duty ratio used by the T-AVM. In order to consider the effect of switching ripples, an approximate ripple function is obtained. An iterative algorithm is proposed for utilization of P-AVM and ripple function for large-signal time-domain transient simulations. A boost converter and a two-level three-phase ac–dc converter are used to validate the performance of the P-AVM in comparison with the T-AVM under large ripple and large disturbance conditions. The detailed models developed in PSCAD/EMTDC are used as benchmarks. Improvement in accuracy is demonstrated. The efficiency of the iterative algorithm is discussed. Experiments on a 50-kVA three-phase ac–dc converter are conducted to validate the proposed method.**

***Index Terms*—Electromagnetic transient analysis, modeling, pulse width modulated power converters, simulation.**

I. Introduction

POWER electronic converters are widely used in modern power systems for various applications, including wind farms, photovoltaic power plants, FACTS devices, HVDC transmission systems, distributed generators, energy storage, microgrids, and plug-in hybrid electric vehicles [1]–[5]. Transient simulation capability is essential for the design, analysis, and control of these power electronics-based systems [6], [7]. With the models of individual switching devices and the topology of power converters, transient simulations can be performed by several simulation tools, e.g., PSCAD/EMTDC [8] and MATLAB/Simulink [9]. However, when the detailed model is adopted, small time steps and/or auxiliary algorithms are required to accurately emulate switching events within the converters [6], [10], [11]. Therefore, it is computationally inefficient to simulate power systems containing a large number of power converters, e.g., large-scale wind farms, using the detailed model.

Dynamic average-value model (AVM) is an effective alternative to the detailed model when the phenomena associated with switching harmonics are not a major concern [12]. Recently, the IEEE Task Force on Dynamic Average Modeling published several papers concerning the definition and applications of dynamic AVMs [12]–[15]. According to [12], using dynamic AVMs can significantly reduce the computation time for both large-signal time-domain transient simulations and small-signal frequency-domain analysis, because large time steps can be adopted and the discontinuity in detailed models caused by switching events is eliminated by averaging.

Generally, dynamic AVMs can be derived by circuit averaging, state-space averaging, or switching-frequency-dependent averaging [7], [12]. Local average [16] over the switching period is used in all these methods. For pulse width modulation (PWM) converters, the switching period equals the period of the sawtooth or triangular carrier waveform. For line-commutated converters, the switching period is associated with the ac line frequency, i.e., 50/60 Hz. For example, the switching period of a two-level three-phase diode rectifier is 1/6 of the ac line period [15].

The circuit averaging method directly averages current and voltage waveforms associated with each component of the converter, resulting in an averaged circuit [17]–[22]. Compared with the original circuit, all linear time-invariant components, such as inductors and capacitors, remain the same in the averaged circuit, while the switches or so-called switching cells [17] are replaced by controlled voltage or current sources [18], [21]–[22], ideal transformers [19], or combinations of them [20].

For the state-space averaging, converters are represented by a set of differential algebraic equations (DAEs), including state equations describing the dynamics of state variables and output equations that formulate the output variables as functions of the input and state variables. The DAEs are discontinuous due to switching events. By applying local average to the DAEs over the switching period, a set of continuous DAEs, i.e., the state-space AVM, is obtained [23]–[27].

Manuscript received November 24, 2014; revised February 9, 2015; accepted April 2, 2015. Date of publication April 13, 2015; date of current version September 29, 2015. This work was supported in part by the NSFC under Grants 51277104 and 51207076, and the Tsinghua University Initiative Scientific Research Program under Grant 20121087926. Recommended for publication by Associate Editor M. Ordonez.

Y. Xu is with the School of Electrical Engineering and Computer Science, Washington State University, Pullman, WA 99164 USA (e-mail: yxu2@eecs.wsu.edu).

Y. Chen and H. Gao are with the Department of Electrical Engineering, Tsinghua University, Beijing 100084, China (e-mail: chen_ying@tsinghua.edu.cn; ghx07@mails.tsinghua.edu.cn).

C.-C. Liu is with the School of Electrical Engineering and Computer Science, Washington State University, Pullman, WA 99164 USA, and also with the School of Mechanical and Materials Engineering, University College Dublin, Dublin, Ireland (e-mail: liu@eecs.wsu.edu).

Color versions of one or more of the figures in this paper are available online at http://ieeexplore.ieee.org.

Digital Object Identifier 10.1109/TPEL.2015.2422291

Switching-frequency-dependent averaging methods, including the generalized averaging (also referred to as the dynamic-phasor-based averaging) [28]–[32], Krylov–Bogoliubov–Mitropolsky (KBM) averaging [33]–[36], and time-invariant multifrequency (TIMF) averaging [36], have been proposed to take into account switching ripples and their effects on the transient characteristics of converters. The generalized averaging expands the waveforms of circuit state variables using Fourier series [28]. The Fourier coefficients are also called the dynamic phasors [29]. By selecting finite terms in the Fourier series and using the corresponding coefficients as state variables, the generalized AVM is represented by a set of differential equations in the state space [28]–[32]. The KBM averaging represents the circuit state variables by a series of piecewise polynomial functions [33]–[35]. Since the waveforms of circuit state variables, such as inductor currents and capacitor voltages, are piecewise exponential, using piecewise polynomial functions would get a better approximation to the ripples than the sinusoidal functions used in the generalized averaging. The TIMF averaging represents the circuit state variables and switching functions by the quasi-Fourier series (QFS) and uses the QFS coefficients as state variables of the corresponding AVM [36]. The TIMF averaging considers the type of carrier waveforms. The construction of the TIMF AVM is easier than that of the generalized AVM and KBM-based AVM, especially for high-order AVMs.

Parasitic elements and conduction losses are ignored in most studies. Efforts have been made by some researchers to consider their effects [37]–[41]. Note that analytically developing AVMs that consider parasitic effects is complicated, especially for high-order converters. An approach that establishes AVMs numerically is proposed in [38] and applied to several dc–dc converters [39], [40]. The numerical AVMs show high accuracy in large-signal time-domain transient simulations as well as small-signal frequency-domain analysis.

This paper is focused on the state-space averaged modeling of PWM converters for large-signal time-domain transient simulations. In the preliminary study, an improved AVM for PWM converters with one group of switches is proposed and integrated into the Electromagnetic Transient Program [42]. This paper provides a generalized methodology. The main contributions are as follows:

1) A piecewise state-space AVM (P-AVM) for PWM converters is proposed. The actual duty ratio over each switching cycle is used as the control input instead of the continuous duty ratio adopted by the traditional state-space AVM (T-AVM).
2) An approximate ripple function is derived to take into account the effect of switching ripples.
3) An iterative algorithm is designed to perform transient simulations with the P-AVM and ripple function. The target system is simulated by switching cycles. Within a switching cycle, simulation is conducted iteratively to accurately determine switching instants.

The remaining of this paper is organized as follows. Section II reviews the T-AVM and demonstrates its limitations. Section III describes the proposed method, including the P-AVM, ripple estimation, and iterative algorithm. In Section IV, simulation results for a boost converter and a two-level three-phase ac–dc converter are analyzed. An experimental validation is presented in Section V. The conclusion is given in Section VI.

II. Averaged Modeling of PWM Converters

A. Switched State-Space Models of PWM Converters

A PWM converter can be modeled by the following discontinuous DAEs:

$$\frac{\mathrm{d}\boldsymbol{x}}{\mathrm{d}t} = \boldsymbol{A}_0\boldsymbol{x} + \boldsymbol{B}_0\boldsymbol{u} + \sum_{i=1}^{p}\left[\left(\boldsymbol{A}_i\boldsymbol{x} + \boldsymbol{B}_i\boldsymbol{u}\right)S_i\right] \tag{1}$$

$$\boldsymbol{y} = \boldsymbol{C}\boldsymbol{x} + \boldsymbol{D}\boldsymbol{u} \tag{2}$$

where t is time; $\boldsymbol{x}$, $\boldsymbol{u}$, and $\boldsymbol{y}$ are state, input, and output vectors, respectively; $\boldsymbol{A}_i$, $\boldsymbol{B}_i$ $(i = 0, 1, \ldots, p)$, $\boldsymbol{C}$, and $\boldsymbol{D}$ are coefficient matrices, whose values depend on the topology and parameters of the converter; S_i $(i = 1, \ldots, p)$ are switching functions; p is the number of independent switch groups; i is the index of switch groups.

The switching function S_i is a binary value function, i.e., $S_i = 0$ or 1. It indicates the status of the corresponding switch group. For PWM converters, the value of S_i is determined by the instantaneous values of the reference and carrier waveforms, i.e.

$$S_i\left(t\right) = \begin{cases} 1, \text{if } V_{f,i}(t) > V_c\left(t\right) \\ 0, \text{if } V_{f,i}(t) \le V_c(t) \end{cases}, \; i = 1, \ldots, p \tag{3}$$

where $V_{f,i}$ is the reference waveform for the *i*th switch group and V_c is the carrier waveform.

B. Traditional State-Space AVM

Define the lagged running average [16]

$$\bar{\boldsymbol{f}}\left(t\right) = \frac{1}{T}\int_{t-T}^{t}\boldsymbol{f}\left(\tau\right)\mathrm{d}\tau \tag{4}$$

where $\boldsymbol{f}$ can be any time-domain variable or vector, $\bar{\boldsymbol{f}}$ is the lagged running average of $\boldsymbol{f}$, and T is the length of averaging window.

Let T be the switching period of the converter. Applying (4) to (1) and (2) yields the T-AVM [7], [12], i.e.

$$\frac{\mathrm{d}\bar{\boldsymbol{x}}}{\mathrm{d}t} = \boldsymbol{A}_0\bar{\boldsymbol{x}} + \boldsymbol{B}_0\bar{\boldsymbol{u}} + \sum_{i=1}^{p}\left[\left(\boldsymbol{A}_i\bar{\boldsymbol{x}} + \boldsymbol{B}_i\bar{\boldsymbol{u}}\right)d_i\right] \tag{5}$$

$$\bar{\boldsymbol{y}} = \boldsymbol{C}\bar{\boldsymbol{x}} + \boldsymbol{D}\bar{\boldsymbol{u}} \tag{6}$$

where $\bar{\boldsymbol{x}}$, $\bar{\boldsymbol{u}}$, and $\bar{\boldsymbol{y}}$ are the averaged state, input, and output vectors, respectively. d_i is called the *continuous duty ratio* [7] for the *i*th switch group, defined by

$$d_i\left(t\right) = \frac{1}{T}\int_{t-T}^{t}S_i\left(\tau\right)\mathrm{d}\tau. \tag{7}$$

Assume that $V_{f,i}$ varies slowly with respect to the switching period and can be considered to be constant within a switching

cycle. Then d_i can be formulated as a function of $V_{f,i}$, i.e.

$$d_i = g\left(V_{f,i}\right). \tag{8}$$

The specific form of g depends on the carrier waveform, e.g., for a sawtooth carrier with a magnitude of F, $d_i = V_{f,i}/F$ [7]; for an isosceles triangular carrier whose maximum and minimum values are 1 and -1, respectively, $d_i = 0.5\left(V_{f,i}+1\right)$ [47]. In transient simulations, the instantaneous value of d_i is calculated from $V_{f,i}$ by (8) rather than using its definition, i.e., (7). As a result, (5) becomes an AVM whose control inputs are $V_{f,i}, i = 1, \ldots, p$.

The accuracy of the T-AVM relies on the assumption of a slowly varying $V_{f,i}$. However, this assumption is invalid under some conditions, as illustrated in the following two sections.

C. Challenges Under Large Ripple Condition

In this paper, the term, "ripple," refers to the switching ripple, i.e., the deviation of a waveform from its average whose frequency is equal to the switching frequency. The challenges for averaged modeling of large-ripple converters have been well analyzed by Lehman *et al.* [33], [43]–[45] and discussed in [46].

Briefly speaking, ignoring ripples causes errors in the switching instants, as well as the continuous duty ratio d_i. Since d_i is the control input of the T-AVM, errors in d_i will reduce the accuracy of the T-AVM in transient simulations. When the ripple is small, its effect is minor and can be neglected, which is an assumption of the T-AVM. However, the switching frequency of practical power converters is limited due to heat removal issues. Low switching frequency may cause large ripples [44]. In this case, ignoring ripples will lead to errors in simulation [33], [43].

Two approaches can be employed to take into account the effect of ripples. One is to use the switching-frequency-dependent averaging with first-order or higher-order approximations [30]. High-order approximations improve the accuracy but require more computational efforts. For example, the number of state variables in a second-order approximation is five times of that in the T-AVM. The other approach is to estimate the ripple waveforms. Based on a linear-ripple assumption, an approximate ripple function is obtained in [33]. It is applied to the averaged modeling of dc–dc converters and a switching frequency dependent AVM is given in [43]. To use this model, explicit expressions of switching instants are required. However, it is difficult to achieve this for most PWM converters with feedback control.

D. Challenges in Simulating Large Disturbances

The T-AVM assumes that $V_{f,i}$ is constant within a switching cycle and varies slowly with switching cycles. Therefore, in the time scale of several switching periods, S_i is nearly *T*-periodic and d_i is nearly constant, as shown in Fig. 1(a). An essential observation in Fig. 1(a) is that the areas under the waveforms of S_i and d_i over a switching cycle are equal, i.e., they have the same integral over a switching cycle.

During large disturbances, state variables may change dramatically, leading to fast deviations in the reference waveforms. As a result, $V_{f,i}$ will not be constant within a switching cycle and S_i will not be *T*-periodic, as shown in Fig. 1(b). Therefore, the relationship between d_i and $V_{f,i}$ defined by (8) no longer stands. It can be validated that S_i and d_i [computed by (8)] have different integrals over a switching cycle in this case. However, according to the definition of d_i given by (7), the integrals of S_i and d_i over any switching cycle should be the same. As a result, using (8) will induce errors in d_i under large-disturbance conditions.

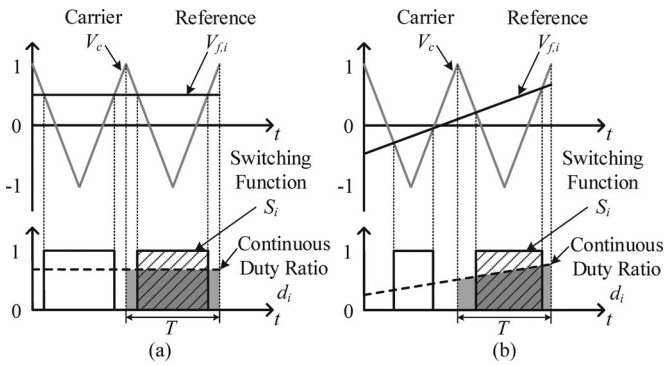

Fig. 1. Waveforms of carrier, reference, switching function, and continuous duty ratio. (a) In steady state or under small-disturbance conditions. (b) Under large-disturbance conditions.

E. Effect of Feedback Controllers

As discussed above, when $V_{f,i}$ has a large ripple or varies fast, errors will be induced in d_i. Model the error as a small disturbance, denoted by $\hat{d}_i$. Suppose that $\hat{d}_i$ causes a deviation in an output variable c_{out}. Let $\hat{c}_{\text{out}}$ denote the deviation of c_{out}. The control-to-output transfer function [48] is used to describe how $\hat{d}_i$ influences $\hat{c}_{\text{out}}$, i.e.

$$G_{cd}\left(s\right) = \frac{\hat{c}_{\text{out}}\left(s\right)}{\hat{d}_i\left(s\right)} \tag{9}$$

where $G_{cd}\left(s\right)$ is the open-loop control-to-output transfer function, s is the Laplace variable.

In practice, most PWM converters are feedback controlled. By modern control theory, feedback controllers can reduce the effect of disturbances [49]. Assume that a feedback controller is used to maintain c_{out} at a desired setpoint. The control-to-output transfer function becomes [48]

$$G'_{cd}\left(s\right) = \frac{G_{cd}\left(s\right)}{1+T\left(s\right)} \tag{10}$$

where $G'_{cd}\left(s\right)$ is the closed-loop control-to-output transfer function, $T\left(s\right)$ is the loop gain, i.e., the product of the gains around the forward and feedback paths of the loop. If the controller is well designed, $||T\left(s\right)|| \gg 1$ at a low frequency, the magnitude of the control-to-output transfer function will be significantly reduced. That is, the effect of disturbance $\hat{d}_i$ on output variable c_{out} is reduced by feedback control.

However, if a large disturbance causes the output of the feedback controller to hit its upper or lower limit, the feedback controller will behave like an open-loop controller. In this case, the performance of the T-AVM will deteriorate.

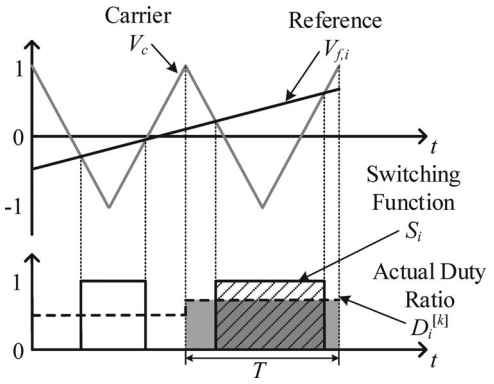

Fig. 2. Illustration of the piecewise averaging.

III. Proposed Modeling and Simulation Method

A. Piecewise Averaging and P-AVM

Suppose that the simulation start time and end time are 0 and $l\,(l>0)$, respectively. Divide the simulation time interval into N switching periods, $[0,T),[T,2T),\ldots,[(N-1)T,NT)$, and a leftover interval $[NT,l]$ shorter than a switching period, where N is the greatest integer less than or equal to l/T. Let k be the index of switching cycles, $1\le k\le N$. The piecewise average of a time-domain variable or vector $\boldsymbol{f}$ is defined by

$$\bar{\boldsymbol{f}}(t)=\frac{1}{T}\int_{(k-1)T}^{kT}\boldsymbol{f}(\tau)\,\mathrm{d}\tau, t\in[(k-1)T,kT) \tag{11}$$

where $\bar{\boldsymbol{f}}$ denotes the piecewise average of $\boldsymbol{f}$. The same notation is used for both the lag running average and piecewise average.

Applying (11) to (1) and (2) yields the piecewise state-space AVM (P-AVM) of PWM converters, i.e.

$$\frac{\mathrm{d}\bar{\boldsymbol{x}}}{\mathrm{d}t}=\boldsymbol{A}_0\bar{\boldsymbol{x}}+\boldsymbol{B}_0\bar{\boldsymbol{u}}+\sum_{i=1}^{p}\left[\left(\boldsymbol{A}_i\bar{\boldsymbol{x}}+\boldsymbol{B}_i\bar{\boldsymbol{u}}\right)D_i^{[k]}\right] \tag{12}$$

$$\bar{\boldsymbol{y}}=\boldsymbol{C}\bar{\boldsymbol{x}}+\boldsymbol{D}\bar{\boldsymbol{u}} \tag{13}$$

where $D_i^{[k]}$ is the *actual duty ratio* [7] in the *k*th switching cycle for the *i*th switch group. For the N switching cycles, $D_i^{[k]}$ is defined by

$$D_i^{[k]}(t)=\frac{1}{T}\int_{(k-1)T}^{kT}S_i(s)\,\mathrm{d}s, t\in[(k-1)T,kT). \tag{14}$$

For the last subinterval $[NT,l]$, however, it is given by

$$D_i^{[N+1]}(t)=\frac{1}{l-NT}\int_{NT}^{l}S_i(s)\,\mathrm{d}s, t\in[NT,l]. \tag{15}$$

$D_i^{[k]}(t)$ is a piecewise constant function of *t*. Its value remains constant within a switching cycle, as shown in Fig. 2.

According to (14), (15), and Fig. 2, the integrals of S_i and $D_i^{[k]}$ over the *k*th switching cycle $[(k-1)T,kT), k=1,\ldots,N$ or the remaining $[NT,l]$ are always equal, whether the reference waveform $V_{f,i}$ is constant or not.

The accuracy of the P-AVM is assured by the following theorem.

Theorem: Let $\boldsymbol{x}(t)$ and $\bar{\boldsymbol{x}}(t)$ be the solution of (1) and (12), respectively. It is given that the switching period $T>0$ and the length of simulation time interval $l>0$. Suppose that $\boldsymbol{x}(0)=\bar{\boldsymbol{x}}(0)$ and $||\boldsymbol{A}_i\boldsymbol{x}(t)+\boldsymbol{B}_i\boldsymbol{u}(t)||\le M_i, i=0,1,\ldots,p$. Then there exists a constant $c>0$ such that

$$||\boldsymbol{x}(t)-\bar{\boldsymbol{x}}(t)||<cT \tag{16}$$

for $t\in[0,l]$, where

$$c=\left(l\sum_{i=0}^{p}M_i\sum_{i=1}^{p}||\boldsymbol{A}_i||+\sum_{i=1}^{p}M_i\right)e^{\sum_{i=0}^{p}||\boldsymbol{A}_i||l}. \tag{17}$$

Proof: Scale time by $\tau=t/T$. Rewriting (1) and (12) in the new time τ, it is obtained that

$$\frac{\mathrm{d}\boldsymbol{x}}{\mathrm{d}\tau}=T\cdot\left\{\boldsymbol{A}_0\boldsymbol{x}+\boldsymbol{B}_0\boldsymbol{u}+\sum_{i=1}^{p}\left[\left(\boldsymbol{A}_i\boldsymbol{x}+\boldsymbol{B}_i\boldsymbol{u}\right)S_i\right]\right\} \tag{18}$$

$$\frac{\mathrm{d}\bar{\boldsymbol{x}}}{\mathrm{d}\tau}=T\cdot\left\{\boldsymbol{A}_0\bar{\boldsymbol{x}}+\boldsymbol{B}_0\bar{\boldsymbol{u}}+\sum_{i=1}^{p}\left[\left(\boldsymbol{A}_i\bar{\boldsymbol{x}}+\boldsymbol{B}_i\bar{\boldsymbol{u}}\right)D_i^{[k]}\right]\right\} \tag{19}$$

The input variables of PWM converters are terminal voltages and/or currents. Suppose that the dc inputs vary slowly and the ac inputs are near-sinusoidal signals of the line frequency, i.e., 50/60 Hz. Normally, the switching frequency is 1 kHz or higher. Therefore, it is reasonable to assume that the input variables are constant within a switching cycle. As a result, $\bar{\boldsymbol{u}}=\boldsymbol{u}$. So $\bar{\boldsymbol{u}}$ in (19) can be replaced by $\boldsymbol{u}$.

Let $\boldsymbol{E}(\tau)=\boldsymbol{x}(\tau)-\bar{\boldsymbol{x}}(\tau)$ denote the error. Subtracting (19) from (18) and integrating, the error is given by

$$\begin{aligned}\boldsymbol{E}(\tau)=\;&T\boldsymbol{A}_0\int_0^{\tau}\boldsymbol{E}(s)\,\mathrm{d}s\\&+T\sum_{i=1}^{p}\left(\boldsymbol{A}_i\int_0^{\tau}\boldsymbol{E}(s)D_i^{[k]}(s)\,\mathrm{d}s\right)\\&+T\sum_{i=1}^{p}\int_0^{\tau}\left(\boldsymbol{A}_i\boldsymbol{x}(s)+\boldsymbol{B}_i\boldsymbol{u}(s)\right)\\&\times\left(S_i(s)-D_i^{[k]}(s)\right)\mathrm{d}s.\end{aligned} \tag{20}$$

Then

$$\begin{aligned}||\boldsymbol{E}(\tau)||\le\;&T\left\|\boldsymbol{A}_0\int_0^{\tau}\boldsymbol{E}(s)\,\mathrm{d}s\right\|\\&+T\left\|\sum_{i=1}^{p}\left(\boldsymbol{A}_i\int_0^{\tau}\boldsymbol{E}(s)D_i^{[k]}(s)\,\mathrm{d}s\right)\right\|\\&+T\left\|\sum_{i=1}^{p}\int_0^{\tau}\left(\boldsymbol{A}_i\boldsymbol{x}(s)+\boldsymbol{B}_i\boldsymbol{u}(s)\right)\right.\\&\left.\times\left(S_i(s)-D_i^{[k]}(s)\right)\mathrm{d}s\right\|.\end{aligned} \tag{21}$$

Obtain an upper limit of the three terms on the right-hand side of (21), respectively. The first term is bounded by

$$\left\|\boldsymbol{A}_0\int_0^{\tau}\boldsymbol{E}(s)\,\mathrm{d}s\right\|\le||\boldsymbol{A}_0||\int_0^{\tau}||\boldsymbol{E}(s)||\mathrm{d}s. \tag{22}$$

Since $\left|D_i^{[k]}\right|<1$, the upper limit of the second term is

$$\left\|\sum_{i=1}^{p}\left(\boldsymbol{A}_i\int_0^{\tau}\boldsymbol{E}(s)\,D_i^{[k]}(s)\,\mathrm{d}s\right)\right\|\le\sum_{i=1}^{p}||\boldsymbol{A}_i||\int_0^{\tau}||\boldsymbol{E}(s)||\mathrm{d}s. \tag{23}$$

The upper limit of the third term is derived as follows. Divide $[0,\tau]$ into switching periods $[0,1),[1,2),\ldots,[m-1,m)$ and a shorter leftover piece $[m,\tau]$. Then

$$\begin{aligned}&\left\|\int_0^{\tau}\left(\boldsymbol{A}_i\boldsymbol{x}(s)+\boldsymbol{B}_i\boldsymbol{u}(s)\right)\left(S_i(s)-D_i^{[k]}(s)\right)\mathrm{d}s\right\|\\&\le\sum_{k=1}^{m}\left\|\int_{k-1}^{k}\left(\boldsymbol{A}_i\boldsymbol{x}(s)+\boldsymbol{B}_i\boldsymbol{u}(s)\right)\left(S_i(s)-D_i^{[k]}(s)\right)\mathrm{d}s\right\|\\&+\left\|\int_m^{\tau}\left(\boldsymbol{A}_i\boldsymbol{x}(s)+\boldsymbol{B}_i\boldsymbol{u}(s)\right)\left(S_i(s)-D_i^{[k]}(s)\right)\mathrm{d}s\right\|.\end{aligned} \tag{24}$$

The integrals of S_i and $D_i^{[k]}$ on $[k-1,k)$ are equal, i.e.

$$\int_{k-1}^{k}\left(S_i(s)-D_i^{[k]}(s)\right)\mathrm{d}s=0. \tag{25}$$

For every $s\in[k-1,k)$

$$\begin{aligned}&||\boldsymbol{x}(s)-\boldsymbol{x}(k-1)||\\&=T\left\|\int_{k-1}^{s}\left\{\boldsymbol{A}_0\boldsymbol{x}(\lambda)+\boldsymbol{B}_0\boldsymbol{u}(\lambda)\right.\right.\\&\left.\left.+\sum_{i=1}^{p}\left[\left(\boldsymbol{A}_i\boldsymbol{x}(\lambda)+\boldsymbol{B}_i\boldsymbol{u}(\lambda)\right)S_i(\lambda)\right]\right\}\mathrm{d}\lambda\right\|\\&\le T\sum_{i=0}^{p}\int_{k-1}^{s}||\boldsymbol{A}_i\boldsymbol{x}(\lambda)+\boldsymbol{B}_i\boldsymbol{u}(\lambda)||\mathrm{d}\lambda\quad(\text{Since}\,|S_i|\le1)\\&\le T\sum_{i=0}^{p}M_i.\end{aligned} \tag{26}$$

Under the assumption that $\boldsymbol{u}=\text{constant}$ on $[k-1,k)$, the following inequalities hold:

$$\begin{aligned}&\left\|\int_{k-1}^{k}\left(\boldsymbol{A}_i\boldsymbol{x}(s)+\boldsymbol{B}_i\boldsymbol{u}(s)\right)\left(S_i(s)-D_i^{[k]}(s)\right)\mathrm{d}s\right\|\\&=\left\|\int_{k-1}^{k}\left[\boldsymbol{A}_i\boldsymbol{x}(s)\left(S_i(s)-D_i^{[k]}(s)\right)\right.\right.\\&\left.\left.-\boldsymbol{A}_i\boldsymbol{x}(k-1)\left(S_i(s)-D_i^{[k]}(s)\right)\right]\mathrm{d}s\right\|\quad[\text{By}(25)]\\&\le||\boldsymbol{A}_i||\int_{k-1}^{k}||\boldsymbol{x}(s)-\boldsymbol{x}(k-1)||\left|S_i(s)-D_i^{[k]}(s)\right|\mathrm{d}s\\&\le T||\boldsymbol{A}_i||\sum_{i=0}^{p}M_i\quad[\text{By}(26)].\end{aligned} \tag{27}$$

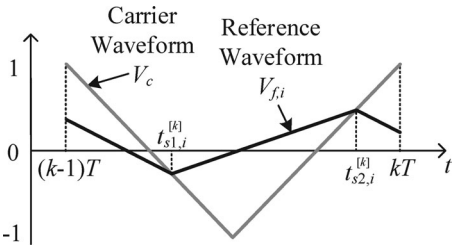

Fig. 3. Triangular carrier waveform, a reference waveform with ripple, and the switching instants.

The first equality holds because $\boldsymbol{B}_i\boldsymbol{u}(s)\left(S_i(s)-D_i^{[k]}(s)\right)$ and $\boldsymbol{A}_i\boldsymbol{x}(k-1)\left(S_i(s)-D_i^{[k]}(s)\right)$ integrate to zero (since $\boldsymbol{u}(s)$ and $\boldsymbol{x}(k-1)$ are constant). The last step uses the fact that $\left|S_i(s)-D_i^{[k]}(s)\right|\le1$ (since $0\le S_i(s),D_i^{[k]}(s)\le1$).

The last integral on the right-hand side of (24) is bounded, i.e.

$$\begin{aligned}&\left\|\int_m^{\tau}\left(\boldsymbol{A}_i\boldsymbol{x}(s)+\boldsymbol{B}_i\boldsymbol{u}(s)\right)\left(S_i(s)-D_i^{[k]}(s)\right)\mathrm{d}s\right\|\\&\le\int_m^{\tau}||\boldsymbol{A}_i\boldsymbol{x}(s)+\boldsymbol{B}_i\boldsymbol{u}(s)||\left|S_i(s)-D_i^{[k]}(s)\right|\mathrm{d}s\\&\le\int_m^{\tau}M_i\mathrm{d}s\\&\le M_i\quad(\text{Since}\,[m,\tau]\,\text{is shorter than 1}).\end{aligned} \tag{28}$$

Substituting (27) and (28) into (24), one obtains the upper limit of the third term on the right-hand side of (21), i.e.

$$\begin{aligned}&\left\|\sum_{i=1}^{p}\int_0^{\tau}\left(\boldsymbol{A}_i\boldsymbol{x}(s)+\boldsymbol{B}_i\boldsymbol{u}(s)\right)\left(S_i(s)-D_i^{[k]}(s)\right)\mathrm{d}s\right\|\\&\le\sum_{i=1}^{p}\left(mT||\boldsymbol{A}_i||\sum_{j=0}^{p}M_j+M_i\right)\\&\le l\sum_{i=0}^{p}M_i\sum_{i=1}^{p}||\boldsymbol{A}_i||+\sum_{i=1}^{p}M_i\quad(\text{Since}\,mT<\tau T\le l).\end{aligned} \tag{29}$$

Substituting (22), (23), and (29) into (21) yields

$$\begin{aligned}||\boldsymbol{E}(\tau)||\le\;&T\sum_{i=0}^{p}||\boldsymbol{A}_i||\int_0^{\tau}||\boldsymbol{E}(s)||\mathrm{d}s\\&+Tl\sum_{i=0}^{p}M_i\sum_{i=1}^{p}||\boldsymbol{A}_i||+T\sum_{i=1}^{p}M_i.\end{aligned} \tag{30}$$

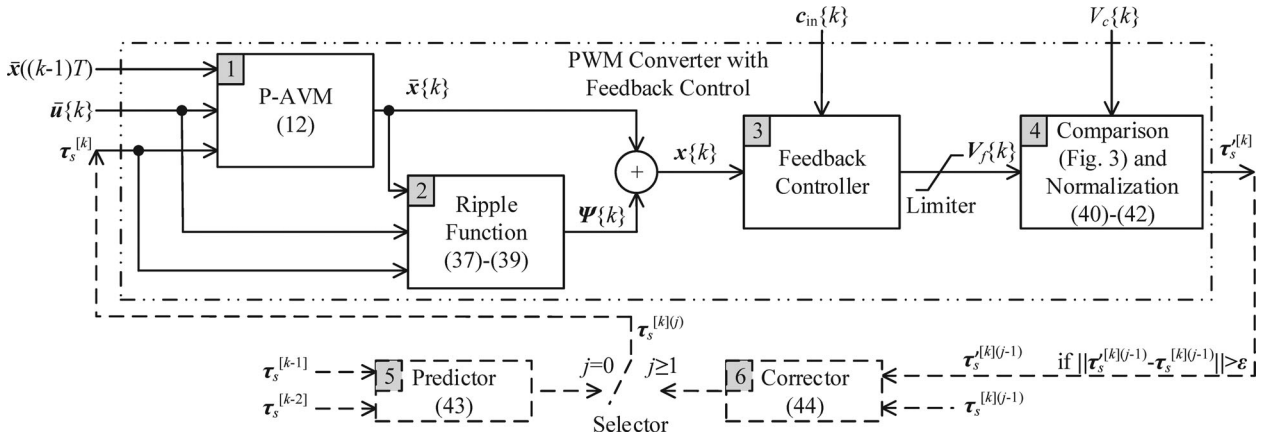

Fig. 4. Model of PWM converters with feedback control and the predictor-corrector iterative algorithm.

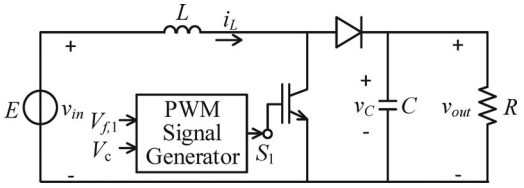

Fig. 5. Boost PWM converter.

Applying the Gronwall's inequality [16] to (30), the boundary of $||\boldsymbol{E}(\tau)||$ is obtained, i.e.

$$||\boldsymbol{E}(\tau)|| \le T\left(l\sum_{i=0}^{p} M_i \sum_{i=1}^{p} ||\boldsymbol{A}_i|| + \sum_{i=1}^{p} M_i\right) e^{\sum_{i=0}^{p} ||\boldsymbol{A}_i|| T\tau}. \tag{31}$$

Note that, for $\tau \in [0, L/T]$, $T\tau \le l$. Therefore, $||\boldsymbol{E}(\tau)|| \le cT$, where c is given by (17). Q.E.D.

By this theorem, $\bar{\boldsymbol{x}} \to \boldsymbol{x}$ when $T \to 0$. It means that the accuracy of the P-AVM improves as the switching frequency increases. The constant c is associated with $||\boldsymbol{A}_i||$ and M_i, which are determined by the topology, parameters, and state of the PWM converter.

In the proof, the input vector $\boldsymbol{u}$ is assumed to be constant within a switching cycle. The assumption is valid in most scenarios of interest, such as startup, load change, adjustment in control reference, and step change in inputs. In these scenarios, $\boldsymbol{u}$ usually varies slowly with respect to the switching period. A step change in $\boldsymbol{u}$ may lead to violation of this assumption in the switching cycle when the change occurs. However, the assumption still holds in other switching cycles. So its influence on the simulation results is minor.

B. Ripple Estimation

The state vector can be formulated by

$$\boldsymbol{x}(t) = \bar{\boldsymbol{x}}(t) + \boldsymbol{\Psi}(t) \tag{32}$$

where $\boldsymbol{\Psi}$ is called the ripple function.

Without loss of generality, consider the kth switching cycle $[(k-1)T, kT)$. Suppose that the triangular waveform in Fig. 3 is used as the carrier waveform. For the ith switch group, there are two switching instants within a switching cycle, denoted by $t_{s1,i}^{[k]}$ and $t_{s2,i}^{[k]}$, respectively.

The method proposed in [33] is used to obtain an approximation of $\boldsymbol{\Psi}$. The following assumptions are made:

1) $\bar{\boldsymbol{u}} = \boldsymbol{u} = \text{constant}$ within a switching cycle;
2) $\bar{\boldsymbol{x}}$ varies slowly with respect to the switching period;
3) the magnitude of ripple is much smaller than the average of state variables, i.e., $||\boldsymbol{\Psi}|| \ll ||\bar{\boldsymbol{x}}||$;
4) the average of $\boldsymbol{\Psi}$ over a switching cycle is zero, i.e.

$$\int_{(k-1)T}^{kT} \boldsymbol{\Psi}(s)\,\mathrm{d}s = 0. \tag{33}$$

Integrating (1) and (12) over $[(k-1)T, t]$ yields

$$\boldsymbol{x}(t) = \boldsymbol{x}((k-1)T) + \int_{(k-1)T}^{t} \left\{\boldsymbol{A}_0\boldsymbol{x}(s) + \boldsymbol{B}_0\boldsymbol{u}(s) + \sum_{i=1}^{p}\left[(\boldsymbol{A}_i\boldsymbol{x}(s) + \boldsymbol{B}_i\boldsymbol{u}(s))S_i(s)\right]\right\}\mathrm{d}s \tag{34}$$

$$\bar{\boldsymbol{x}}(t) = \bar{\boldsymbol{x}}((k-1)T) + \int_{(k-1)T}^{t} \left\{\boldsymbol{A}_0\bar{\boldsymbol{x}}(s) + \boldsymbol{B}_0\bar{\boldsymbol{u}}(s) + \sum_{i=1}^{p}\left[(\boldsymbol{A}_i\bar{\boldsymbol{x}}(s) + \boldsymbol{B}_i\bar{\boldsymbol{u}}(s))D_i^{[k]}(s)\right]\right\}\mathrm{d}s. \tag{35}$$

Since $\bar{\boldsymbol{u}} = \boldsymbol{u} = \text{constant}$ on $[(k-1)T, kT)$, a substitution of (32) into (34) yields

$$\begin{aligned}\bar{\boldsymbol{x}}(t) + \boldsymbol{\Psi}(t) &= \bar{\boldsymbol{x}}((k-1)T) + \boldsymbol{\Psi}((k-1)T) \\ &+ \int_{(k-1)T}^{t} \left\{\boldsymbol{A}_0\bar{\boldsymbol{x}}(s) + \boldsymbol{B}_0\bar{\boldsymbol{u}}(s) + \sum_{i=1}^{p}\left[(\boldsymbol{A}_i\bar{\boldsymbol{x}}(s) + \boldsymbol{B}_i\bar{\boldsymbol{u}}(s))S_i(s)\right]\right\}\mathrm{d}s \\ &+ \int_{(k-1)T}^{t} \left[\boldsymbol{A}_0\boldsymbol{\Psi}(s) + \sum_{i=1}^{p}(\boldsymbol{A}_i\boldsymbol{\Psi}(s)S_i(s))\right]\mathrm{d}s. \end{aligned} \tag{36}$$

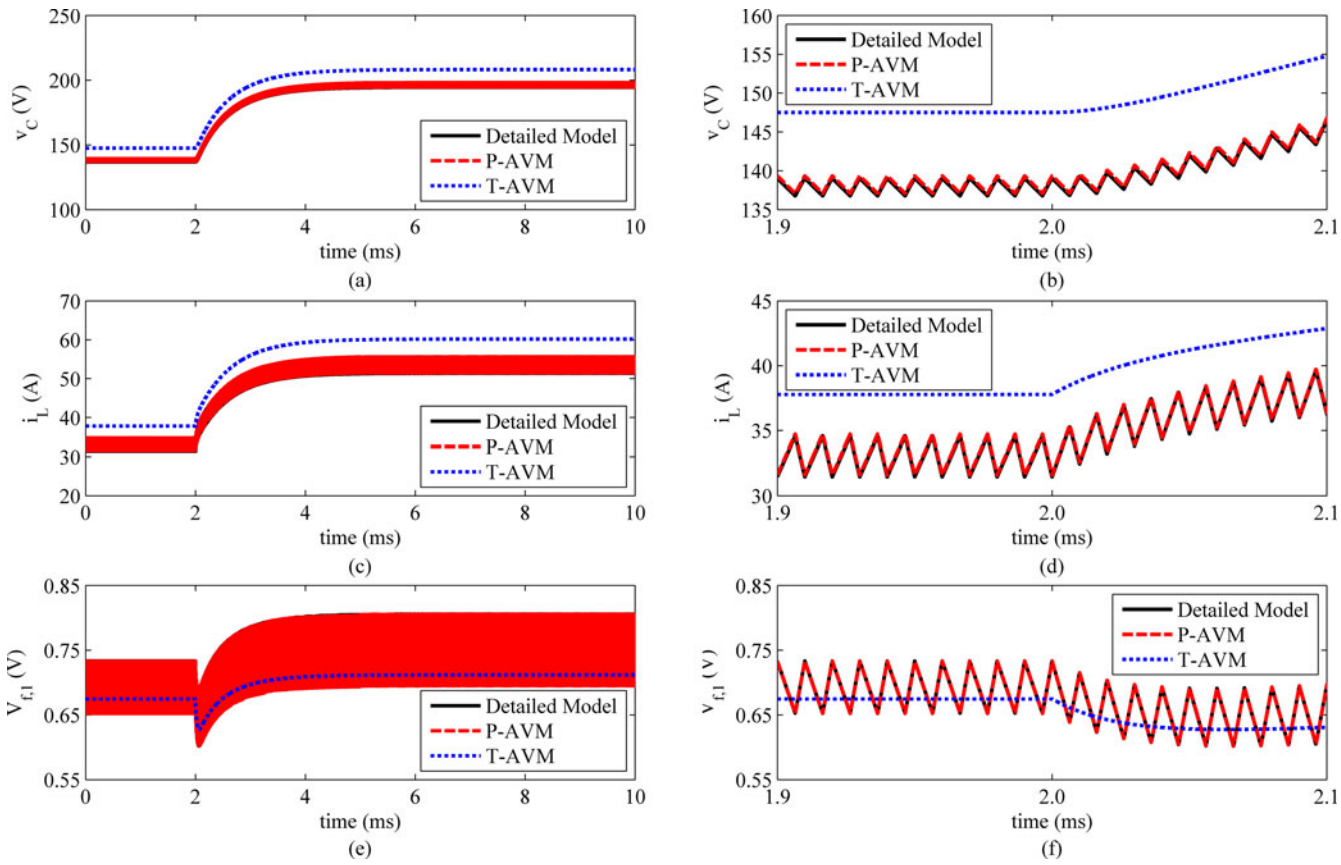

Fig. 6. Response to step change in E: waveforms of (a) ν_c (overall), (b) ν_c (zoomed in), (c) i_L (overall), (d) i_L (zoomed in), (e) $V_{f,1}$ (overall), and (f) $V_{f,1}$ (zoomed in). The reference signal is generated by (45).

Since $||\boldsymbol{\Psi}|| \ll ||\bar{\boldsymbol{x}}||$, the last term on the right-hand side of (36) is ignored. Taking the difference between (36) from (35) and integrating, it is obtained that

$$\boldsymbol{\Psi}(t) = \boldsymbol{\Psi}((k-1)T) + \sum_{i=1}^{p}\left[\left(\boldsymbol{A}_i\bar{\boldsymbol{x}}(t) + \boldsymbol{B}_i\bar{\boldsymbol{u}}(t)\right)\Gamma_i^{[k]}(t)\right] \tag{37}$$

where

$$\Gamma_i^{[k]}(t) = \begin{cases} -D_i^{[k]}t + (k-1)TD_i^{[k]}, & (k-1)T \le t < t_{s1,i}^{[k]} \\ \left(1-D_i^{[k]}\right)t + (k-1)TD_i^{[k]} - t_{s1,i}^{[k]}, & t_{s1,i}^{[k]} \le t < t_{s2,i}^{[k]} \\ -D_i^{[k]}t + kTD_i^{[k]}, & t_{s2,i}^{[k]} \le t < kT. \end{cases} \tag{38}$$

Substituting (37) into (33), integrating, and solving for $\boldsymbol{\Psi}((k-1)T)$, it is shown that

$$\begin{aligned}\boldsymbol{\Psi}((k-1)T) = \frac{1}{2}\sum_{i=1}^{p}\Big\{&\left(\boldsymbol{A}_i\bar{\boldsymbol{x}}((k-1)T)\right. \\ &\left.+\boldsymbol{B}_i\bar{\boldsymbol{u}}((k-1)T)\right) \\ &\cdot\left[t_{s1,i}^{[k]} + t_{s2,i}^{[k]} - (2k-1)T\right]\cdot D_i^{[k]}\Big\}.\end{aligned} \tag{39}$$

(37)–(39) give the approximation of $\boldsymbol{\Psi}$. It is derived by assuming a triangular carrier waveform. However, it can also be applied to a sawtooth carrier waveform, by setting $t_{s1,i}^{[k]} = (k-1)T$.

C. Iterative Algorithm

According to (12) and (37)–(39), $t_{s1,i}^{[k]}$ and $t_{s2,i}^{[k]}$ are the control inputs of the P-AVM and ripple function ($D_i^{[k]}$ can be determined by $D_i^{[k]} = \left(t_{s2,i}^{[k]} - t_{s1,i}^{[k]}\right)/T$). The values of $t_{s1,i}^{[k]}$ and $t_{s2,i}^{[k]}$ change with switching cycles, so they need to be updated at the beginning of each switching cycle.

Normalizing $t_{s1,i}^{[k]}$ and $t_{s2,i}^{[k]}$ by

$$\tau_{s1,i}^{[k]} = \frac{t_{s1,i}^{[k]}}{T} - (k-1) \tag{40}$$

$$\tau_{s2,i}^{[k]} = \frac{t_{s2,i}^{[k]}}{T} - (k-1) \tag{41}$$

it can be proven that $0 \le \tau_{s1,i}^{[k]}, \tau_{s2,i}^{[k]} \le 1$.

Define the normalized switching instants vector by

$$\boldsymbol{\tau}_s^{[k]} = \left[\tau_{s1,1}^{[k]}, \tau_{s2,1}^{[k]}, \ldots, \tau_{s1,i}^{[k]}, \tau_{s2,i}^{[k]}, \ldots, \tau_{s1,p}^{[k]}, \tau_{s2,p}^{[k]}\right]^T. \tag{42}$$

For open-loop controlled converters, the reference waveform $V_{f,i}$ is predefined. Therefore, $t_{s1,i}^{[k]}$ and $t_{s2,i}^{[k]}$ can be obtained by comparing $V_{f,i}$ and V_c. Then $\boldsymbol{\tau}_s^{[k]}$ is determined by (40)–(42).

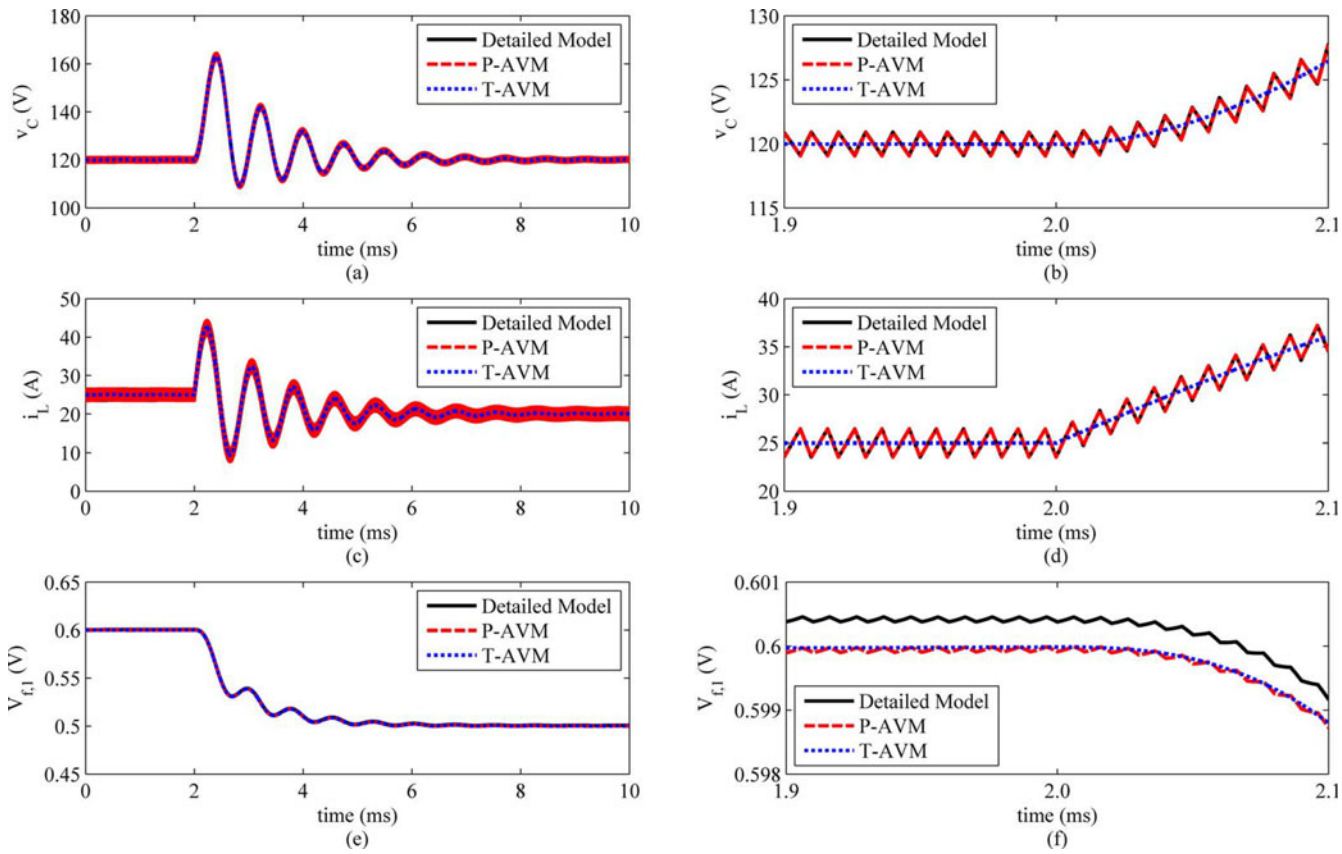

Fig. 7. Response to step change in E waveforms of (a) v_C (overall), (b)v_C (zoomed in), (c) i_L (overall), (d)i_L (zoomed in), (e) $V_{f,1}$ (overall), and (f)$V_{f,1}$ (zoomed in). The reference signal is generated by (46).

For converters with feedback control, $\boldsymbol{\tau}_s^{[k]}$ is associated with $\boldsymbol{x}$, $\boldsymbol{u}$, $\boldsymbol{c}_{\text{in}}$, and V_c, as shown by Blocks 1–4 in Fig. 4. $\boldsymbol{c}_{\text{in}}$ is the reference input vector for the controller. $\boldsymbol{V}_f$ is the vector of the reference waveforms, i.e., $\boldsymbol{V}_f = [V_{f,1}, V_{f,2}, \ldots, V_{f,p}]^T$. The notation $\boldsymbol{f}\{k\}$ denotes the values of $\boldsymbol{f}$ over the kth switching cycle $[(k-1)T, kT)$. Block 1 represents the P-AVM. Given its electrical input $\bar{\boldsymbol{u}}\{k\}$, control input $\boldsymbol{\tau}_s^{[k]}$, and the initial value of averaged state vector $\bar{\boldsymbol{x}}((k-1)T)$, the P-AVM is solved over $[(k-1)T, kT)$ and $\bar{\boldsymbol{x}}\{k\}$ is obtained. Using $\bar{\boldsymbol{u}}\{k\}$, $\boldsymbol{\tau}_s^{[k]}$, and $\bar{\boldsymbol{x}}\{k\}$ as inputs to the ripple function (Block 2) yields $\boldsymbol{\Psi}\{k\}$. Then $\boldsymbol{x}\{k\}$ is obtained by $\boldsymbol{x}\{k\} = \bar{\boldsymbol{x}}\{k\} + \boldsymbol{\Psi}\{k\}$. The feedback controller (Block 3 and the limiter) takes $\boldsymbol{c}_{\text{in}}\{k\}$ and $\boldsymbol{x}\{k\}$ as inputs and provides $\boldsymbol{V}_f\{k\}$ as the output. Block 4 determines a new value of $\boldsymbol{\tau}_s^{[k]}$, denoted by $\boldsymbol{\tau'}_s^{[k]}$ by comparing $\boldsymbol{V}_f$ and V_c. If the given value of $\boldsymbol{\tau}_s^{[k]}$ is accurate, $\boldsymbol{\tau'}_s^{[k]} = \boldsymbol{\tau}_s^{[k]}$.

For most feedback controlled PWM converters, it is infeasible to solve for $\boldsymbol{\tau}_s^{[k]}$ analytically. An iterative algorithm is proposed, as shown by Blocks 5 and 6 and the dashed lines in Fig. 4, where j is the iteration index. Let $\boldsymbol{\tau}_s^{[k](0)}$ denote the initial value and $\boldsymbol{\tau}_s^{[k](j)}$ denote the value of $\boldsymbol{\tau}_s^{[k]}$ at the jth iteration. The iterative procedure is given below.

Step 1: Let $j = 0$ and set an initial value $\boldsymbol{\tau}_s^{[k](0)}$. Linear extrapolation is used to determine $\boldsymbol{\tau}_s^{[k](0)}$ from its values in the previous switching cycles, i.e.

$$\boldsymbol{\tau}_s^{[k](0)} = 2\boldsymbol{\tau}_s^{[k-1]} - \boldsymbol{\tau}_s^{[k-2]}. \tag{43}$$

For the first two switching cycles, let $\boldsymbol{\tau}_s^{[1](0)} = \boldsymbol{0}$ and $\boldsymbol{\tau}_s^{[2](0)} = \boldsymbol{\tau}_s^{[1]}$, respectively.

Step 2: Update the coefficients of the P-AVM and ripple function, perform transient simulation over the kth switching cycle, and compute $\boldsymbol{\tau'}_s^{[k](j)}$.

Step 3: If $||\boldsymbol{\tau'}_s^{[k](j)} - \boldsymbol{\tau}_s^{[k](j)}|| < \varepsilon$, where ε is a small positive number, move to the next switching cycle; otherwise, let $j = j + 1$ and

$$\boldsymbol{\tau}_s^{[k](j)} = \boldsymbol{\tau}_s^{[k](j-1)} + \alpha \cdot \left(\boldsymbol{\tau'}_s^{[k](j-1)} - \boldsymbol{\tau}_s^{[k](j-1)}\right) \tag{44}$$

where α is a positive number, go to Step 2.

When the iterative process converges, the simulation over the kth switching cycle is completed.

IV. Case Study

A. Boost Converter

A boost converter is shown in Fig. 5. It takes a dc voltage source as input and serves a resistive load. There is only one group of switches, i.e., a transistor and a diode, so $p = 1$. The

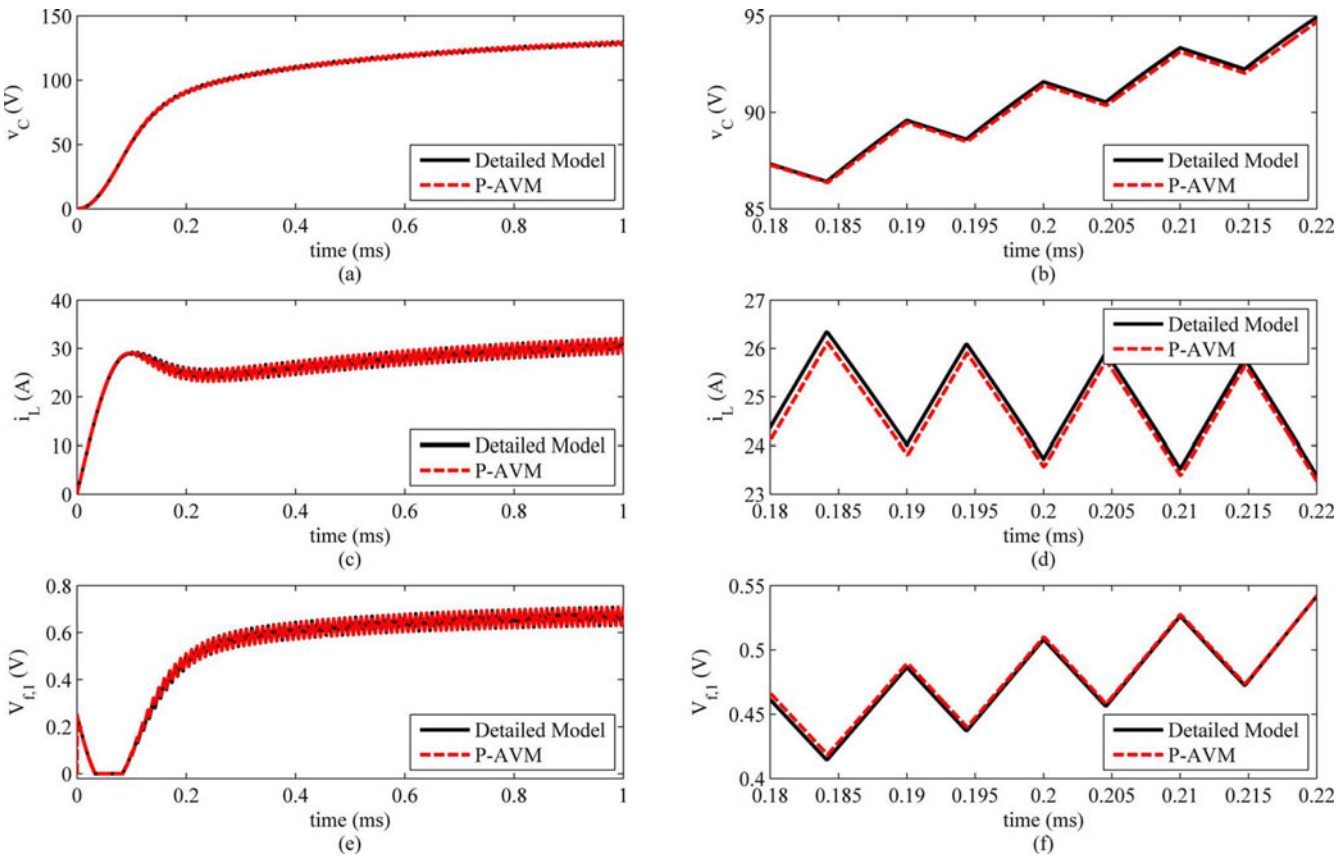

Fig. 8. Startup transients: waveforms of (a) v_C (overall), (b) v_C (zoomed in), (c) i_L (overall), (d) i_L (zoomed in), (e) $V_{f,1}$ (overall), and (f) $V_{f,1}$ (zoomed in).

gate signal of the transistor S_1 is provided by a PWM signal generator. The carrier V_c is a 100-kHz sawtooth waveform whose magnitude is 1 V. The reference waveform $V_{f,1}$ is determined by a feedback controller. Two controllers are considered in this study. One is a linear state feedback controller formulated by [33]

$$V_{f,1} = V_1 - k_1 i_L - k_2 v_C \tag{45}$$

where V_1 is the reference input; $\boldsymbol{k} = [k_1, k_2]$ is the feedback coefficient vector. The other is a PI controller that maintains v_C at a desired value, i.e.

$$V_{f,1} = \left(K_p + \frac{1}{sT_i}\right)(V_2 - Hv_C) \tag{46}$$

where V_2 is the reference input; H is the sensor gain; K_p and T_i are the proportional gain and integral time contant of the PI controller, respectively. For both controllers, the upper limit of $V_{f,1}$ is set to 1 to avoid overmodulation. The parameters of the boost converter and both controllers are given in the Appendix.

Three models are used to simulate the converter:

1) a detailed model developed in PSCAD/EMTDC;
2) a T-AVM developed in PSCAD/EMTDC;
3) a P-AVM (with ripple function) developed using the MATLAB language.

The iterative algorithm proposed in Section III-C is used to simulate the P-AVM. The coefficient α on the right-hand side of (44) is 0.4. The tolerance is specified as $\varepsilon = 0.001$.

Assume that the converter operates in a steady state at the beginning. The source voltage E suddenly increases from 48 to 60 V at $t = 2$ ms. The response of the boost converter with the feedback controller formulated by (45) and (46) is shown in Figs. 6 and 7, respectively.

By comparing Figs. 6 and 7, it can be seen that, the performance of the T-AVM depends on the feedback controller.

In a steady state, the capacitor voltage and inductor current are

$$v_C = \frac{E}{1-d_1}, i_L = \frac{E}{R(1-d_1)^2}. \tag{47}$$

When (45) is used to determine $V_{f,1}$, the steady-state value of d_1 can be obtained by solving the following equation [43]:

$$d_1 = V_1 - k_1 \frac{E}{R(1-d_1)^2} - k_2 \frac{E}{1-d_1} - \delta \tag{48}$$

where

$$\delta = \frac{TEd_1}{2}\left(\frac{k_1}{L} - \frac{k_2}{RC(1-d_1)}\right) \tag{49}$$

represents the effect of ripples.

The T-AVM assumes that the switching frequency is sufficiently high, i.e., $T \to 0$, so $\delta \to 0$. As a result, the ripples are omitted and the last term δ on the right-hand side of (48) is removed.

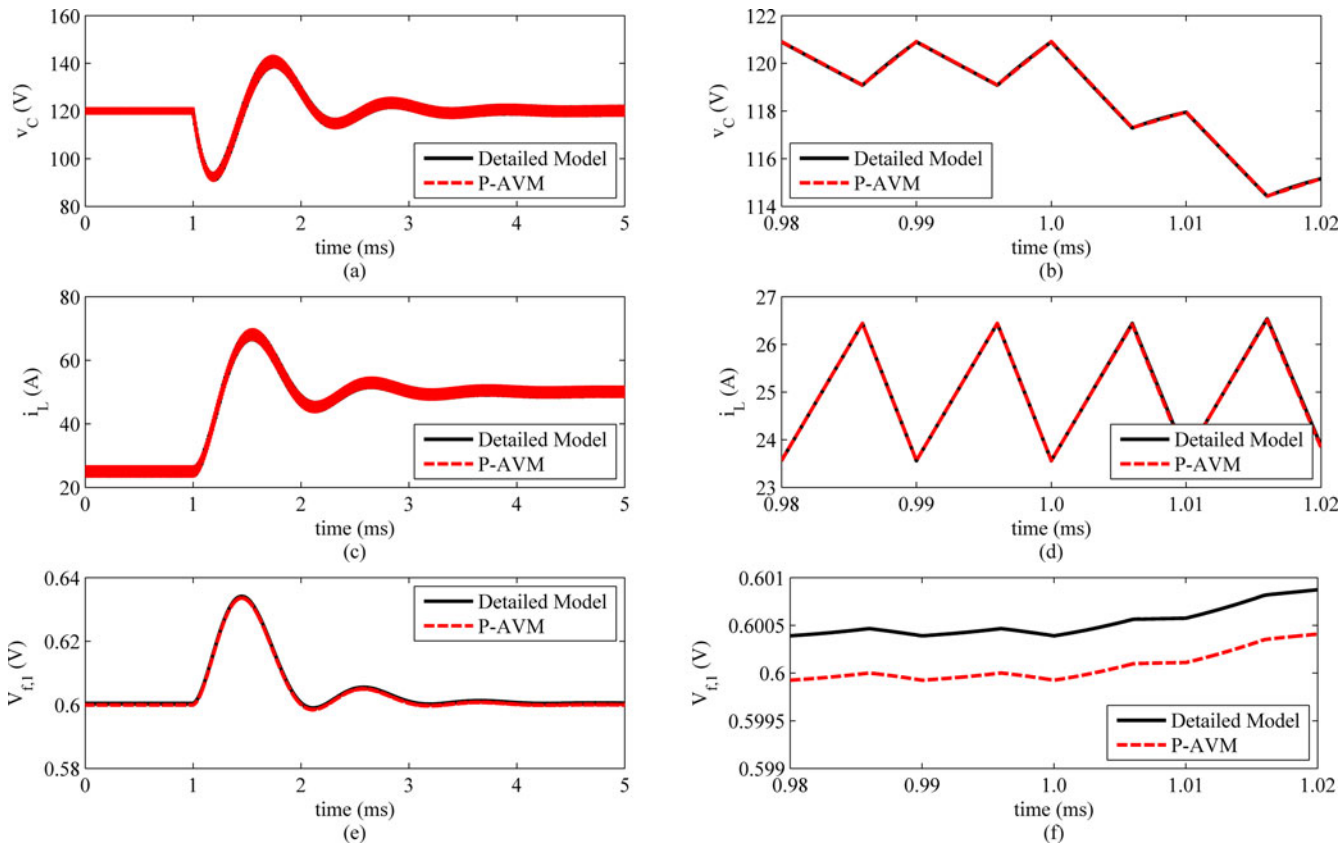

Fig. 9. Response to load change: waveforms of (a) v_C (overall), (b) v_C (zoomed in), (c) i_L (overall), (d) i_L (zoomed in), (e) $V_{f,1}$ (overall), and (f) $V_{f,1}$ (zoomed in).

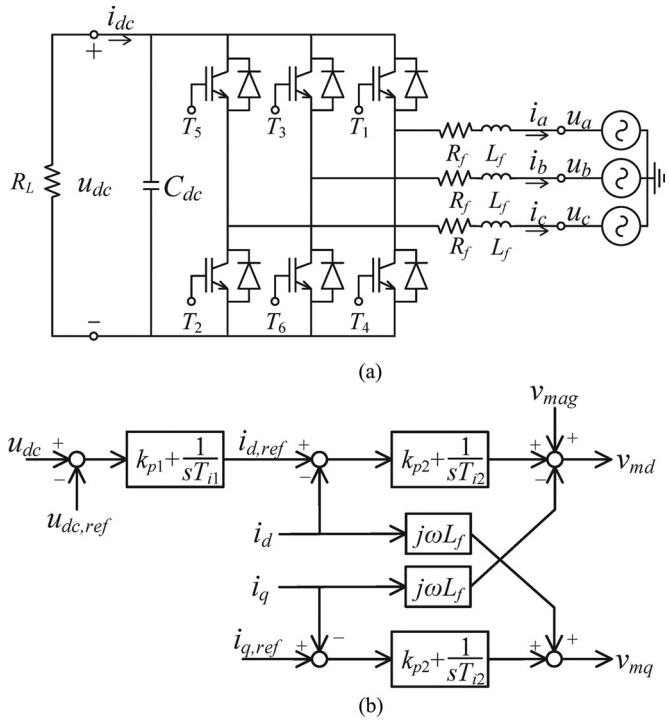

Fig. 10. Two-level three-phase ac-dc converter with a feedback controller. (a) Topology of the converter. (b) Structure of the feedback controller. Voltages and currents are in per unit.

Solving (48) with and without the term δ, the steady-state value of d_1 at $t = 0$ s is obtained as 0.6523 and 0.6746, respectively. The corresponding output voltages are 138.05 and 147.51 V, respectively. Ignoring ripples causes an error of around 8.5 V in the output voltage.

When (46) is used, $v_{\text{out}} = V_2/H = 120$ V in a steady state, whether or not the ripples are considered. The PI controller eliminates steady-state errors.

In a transient state, the PI controller can also reduce the effect of disturbances in d_1 caused by ripples, as illustrated in Section II-E. In this case, $c_{\text{out}} = v_{\text{out}}$ and $T(s)$ is given by

$$T(s) = H\left(K_p + \frac{1}{sT_i}\right) G_{cd}(s). \tag{50}$$

At a low frequency, $||1/sT_i||$ is large, so $||T(s)||$ is also large. Consequently, the closed-loop control-to-output transfer function $G'_{cd}(s)$ defined by (10) is small in magnitude. It means that the disturbance in d_1 has a minor effect on v_{out}. That is why the T-AVM performs well in this case.

The P-AVM matches the detailed model no matter which controller is used. The effects of ripples are taken into account by the ripple function. The proposed iterative algorithm ensures that an accurate value of $D_1^{[k]}$ is obtained over each switching cycle.

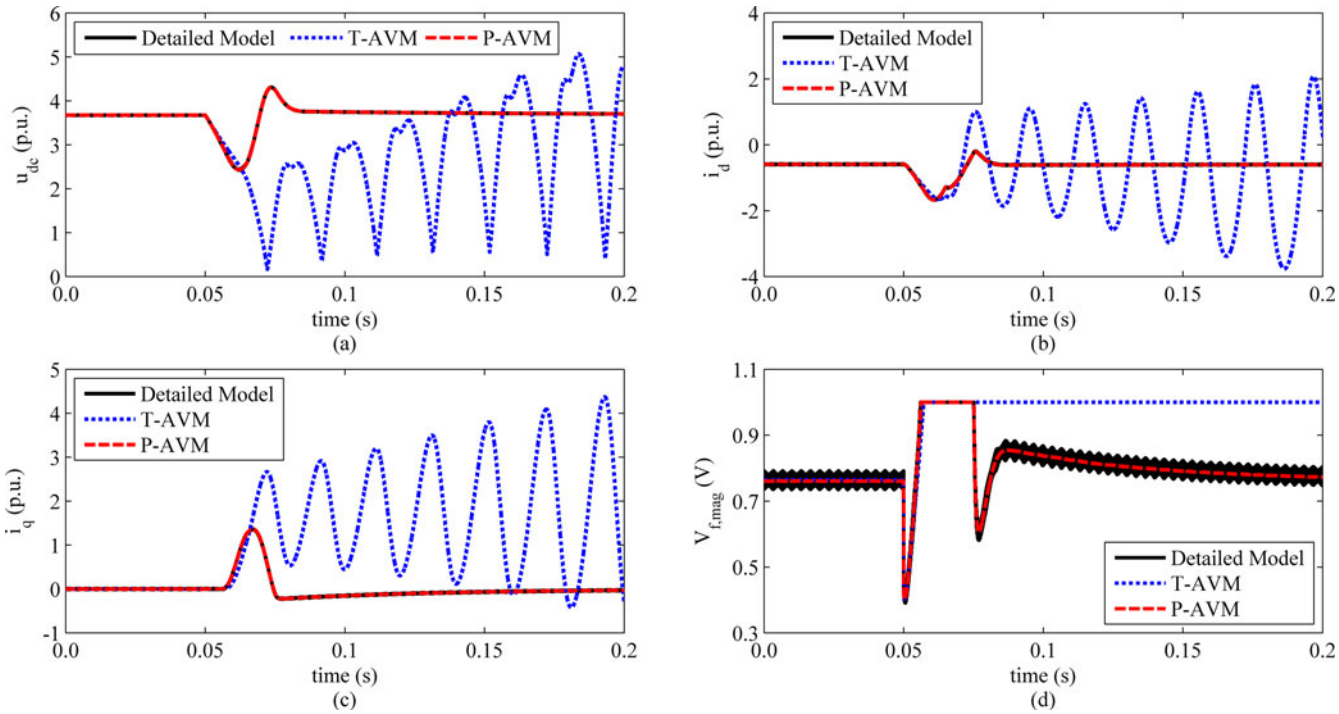

Fig. 11. Response of the three-phase ac-dc converter to a grid voltage drop. Waveforms of (a) $u_{\rm dc}$, (b) i_d, (c) i_q, and (d) $V_{f,\rm mag}$.

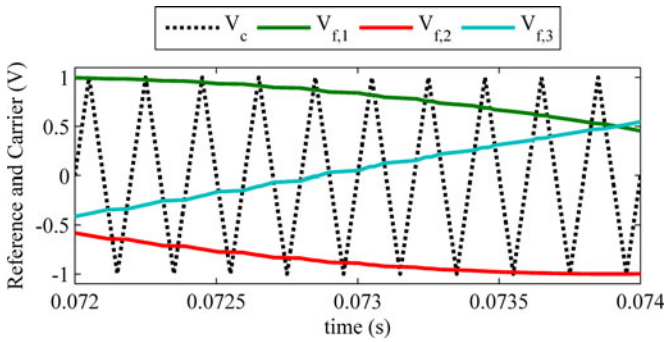

Fig. 12. Carrier and reference waveforms over the time interval [0.072, 0.074] obtained by simulating the detailed model.

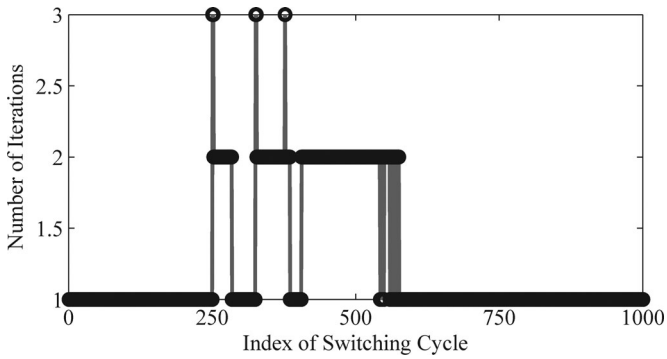

Fig. 13. Number of iterations over each switching cycle.

The startup and load change transients are simulated to further evaluate the accuracy of the P-AVM.

Assume that the initial values of v_C and i_L are zero and (45) is used to determine $V_{f,1}$. The startup of the boost converter is simulated by the detailed model and P-AVM, respectively. The waveforms of v_C, i_L, and $V_{f,1}$ are shown in Fig. 8.

Suppose that the boost converter serves a 12 Ω resistive load at the beginning and (46) is used to determine $V_{f,1}$. At $t = 1$ ms, another 12 Ω resistive load is connected in parallel to the original load. The response of the converter is simulated by the detailed model and P-AVM, respectively. The results are shown in Fig. 9.

From Figs. 8 and 9, it can be seen that the P-AVM matches the detailed model in both scenarios.

B. Two-Level Three-Phase AC–DC Converter

A two-level three-phase ac–dc converter with a feedback controller is shown in Fig. 10. The ac and dc sides of the converter are connected to an ideal three-phase voltage source (representing the power grid) and a resistor, respectively. The feedback controller is designed to maintain the dc-side voltage and ensure that the converter exchanges only active power with the grid. Vector control technique is used in a synchronous rotating *dq*-reference frame with its *d*-axis oriented along the grid voltage phasor. Parameters of the converter and its controller are given in the Appendix.

There are three groups of switches, so $p = 3$. Each switch group contains two IGBTs and two antiparallel diodes in the same phase, as shown in Fig. 10(a). Let the index $i = 1$, 2, and 3 denote phase *a*, *b*, and *c*, respectively. The switching signals are generated by a sinusoidal PWM signal generator. A 5-kHz triangular waveform with a magnitude of 1 V is used as the carrier, as shown in Fig. 3. The reference waveforms for phase

TABLE I
ABSOLUTE ERRORS IN STATE VARIABLES

Detailed Model								
State Variable	Time Step (μs)	1 (Benchmark)	10	20	50	100	200	400
$u_{\rm dc}$	Maximum Error (p.u.)	0	0.0089	0.0907	0.1176	2.0199	—	—
	Mean Error (p.u.)	0	0.0011	0.0071	0.0137	0.2054	—	—
i_d	Maximum Error (p.u.)	0	0.0163	0.1276	0.1893	1.9673	—	—
	Mean Error (p.u.)	0	0.0017	0.0089	0.0182	0.2002	—	—
i_q	Maximum Error (p.u.)	0	0.0126	0.1225	0.1463	1.9976	—	—
	Mean Error (p.u.)	0	0.0019	0.0068	0.0192	0.1972	—	—
P-AVM								
State Variable	Time Step (μs)	1	10	20	50	100	200	400
$u_{\rm dc}$	Maximum Error (p.u.)	0.0191	0.0237	0.0352	0.0612	0.1116	0.2228	0.5304
	Mean Error (p.u.)	0.0016	0.0021	0.0030	0.0054	0.0106	0.0218	0.0533
i_d	Maximum Error (p.u.)	0.0161	0.0253	0.0409	0.0771	0.1533	0.3010	0.6928
	Mean Error (p.u.)	0.0039	0.0040	0.0047	0.0052	0.0104	0.0177	0.0403
i_q	Maximum Error (p.u.)	0.0180	0.0305	0.0486	0.0926	0.1734	0.3321	0.7916
	Mean Error (p.u.)	0.0034	0.0041	0.0055	0.0100	0.0191	0.0378	0.0853

a, *b*, and *c* are given by

$$\begin{aligned} V_{f,1} &= V_{f,\rm mag}\sin(\phi_f) \\ V_{f,2} &= V_{f,\rm mag}\sin(\phi_f - 120^\circ) \\ V_{f,3} &= V_{f,\rm mag}\sin(\phi_f + 120^\circ) \end{aligned} \tag{51}$$

where $V_{f,\rm mag}$ and ϕ_f are the magnitude and angle of the reference phasor, respectively. $V_{f,\rm mag}$ is also referred to as the modulation index magnitude [47]. The instantaneous values of $V_{f,\rm mag}$ and ϕ_f are determined by

$$V_{f,\rm mag} = \min\left\{\frac{2\sqrt{v_{md}^2 + v_{mq}^2}}{u_{\rm dc}}, 1\right\} \tag{52}$$

$$\phi_f = \tan^{-1}\frac{v_{mq}}{v_{md}} + \phi_g \tag{53}$$

where v_{md} and v_{mq} are outputs of the feedback controller, as shown in Fig. 10(b); $u_{\rm dc}$ is the dc-side voltage of the converter in per unit; ϕ_g is the angle of the grid voltage phasor. The upper limit of $V_{f,\rm mag}$ is set to 1 to avoid overmodulation.

The converter's response to a grid voltage sag is simulated using the detailed model, T-AVM, and P-AVM, respectively. The simulation time length and time step are 0.2 s and 1 μs, respectively. The coefficient of (44) is $\alpha = 0.9$. The tolerance for the iterative algorithm is $\varepsilon = 0.0016$. Assume the converter operates in a steady state in the beginning and the magnitude of the grid voltage suddenly drops by 70% (30% remaining) at $t = 0.05$ s and recovers to its nominal value after 15 ms. The waveforms of $u_{\rm dc}$, i_d, i_q, and $V_{f,\rm mag}$ are given in Fig. 11.

In this case, $V_{f,\rm mag}$ reaches its upper limit at $t = 0.0563$ s and remains constant for 19 ms (according to the simulation results of the detailed model). It can be seen from Fig. 11 that, before $V_{f,\rm mag}$ reaches its upper limit, both the T-AVM and P-AVM match the detailed model. However, the $u_{\rm dc}$ waveform provided by the T-AVM starts to drift off course and diverges after $V_{f,\rm mag}$ hits the limit. This is because the instantaneous values of the reference waveforms vary fast and cannot be considered a constant within a switching cycle, as shown in Fig. 12. Moreover, the feedback controller has limited effect on rejecting disturbances when $V_{f,\rm mag}$ reaches its upper limit, as illustrated in Section II-E.

The efficiency of the proposed iterative algorithm is analyzed as follows. Define the number of iterations over a switching cycle as the number of times the converter is simulated over the switching cycle, denoted by N_i. For an algorithm without iteration, $N_i \equiv 1$. The curve of N_i versus the switching cycle index is shown in Fig. 13. It can be seen that, in a steady state, $N_i = 1$, which means the switching instants can be accurately predicted by (43). In a transient state, the iterative algorithm converges in two iterations ($N_i = 2$) in most cases. Over the entire simulation time interval, the average value of N_i is 1.257. It means that the amount of calculation increases by 25.7% due to iterations in this case.

In order to evaluate the performance of the P-AVM under large-time-step conditions, set the time step to 1, 10, 20, 50, 100, 200, and 400 μs, respectively. For each time step setting, the detailed model (in PSCAD/EMTDC) and P-AVM (in a C++ program developed by the authors) are used to simulate the grid-voltage-sag scenario discussed above, respectively. The simulation results of the detailed model with a 1-μs time step are used as benchmark. Absolute errors in per unit are calculated for the state variables, i.e., $u_{\rm dc}$, i_d, and i_q. Maximum errors and mean errors over the simulation time interval are considered. The results are given in Table I. The waveforms of state variables are shown in Fig. 14.

The detailed model works well with a time step of 50 μs or smaller. When a 100-μs time step is used, its maximum and mean errors exceed 2 and 0.2 p.u., respectively, and the waveforms of the state variables deviate dramatically from the benchmark, as shown in Fig. 14(a), (c), and (e). In contrast, the waveforms obtained by the P-AVM approximately match the benchmark,

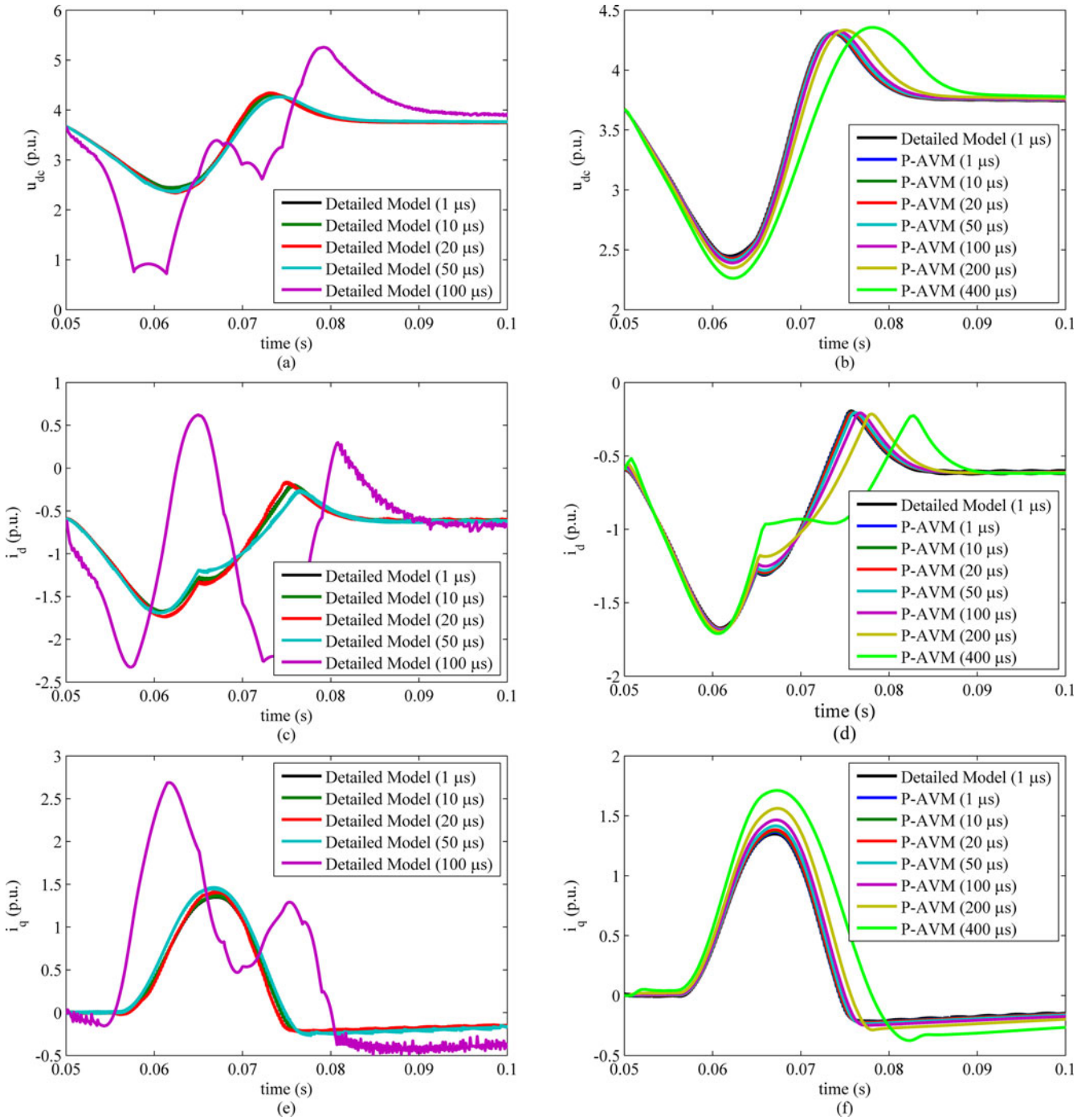

Fig. 14. Waveforms of state variables: (a) u_{dc} (detailed model), (b) u_{dc} (P-AVM), (c) i_d (detailed model), (d) i_d (P-AVM), (e) i_q (detailed model), and (f) i_q (P-AVM).

even if a 400-μs time step is used, as shown in Fig. 14(b), (d), and (f). When a large time step is used, the fluctuation in state variables predicted by the P-AVM is larger than the benchmark in magnitude. A lag in the transient response is also observed. Indeed, using a large time step reduces the sampling rate and increases the response time of the feedback controller. Therefore, the feedback controller cannot follow the fast transient caused by the disturbance. That is, a delay in regulating actions is introduced. One way to refine the simulation results is to add a compensator in the control loop to reduce the impact of delay. Further studies are needed.

The execution time for the simulations with the detailed model and P-AVM are measured and shown in Table II and Fig. 15. For the detailed model, the execution time is reduced in a sublinear speed with the augment of time step. That is, when the time step doubles, the execution time is reduced by less than 50%. This is because the detailed model needs to deal with individual switching events and the number of switching

TABLE II
EXECUTION TIME OF SIMULATIONS

Time Step (μs)		1	10	20	50	100	200	400
Execution Time of	Detailed Model (s)	10.000	1.300	0.790	0.620	0.440	—	—
	P-AVM (s)	6.623	0.526	0.269	0.083	0.040	0.024	0.021
Average Number of Iterations ($N_{i,\mathrm{ave}}$) for P-AVM		1.257	1.257	1.251	1.273	1.246	1.229	2.046

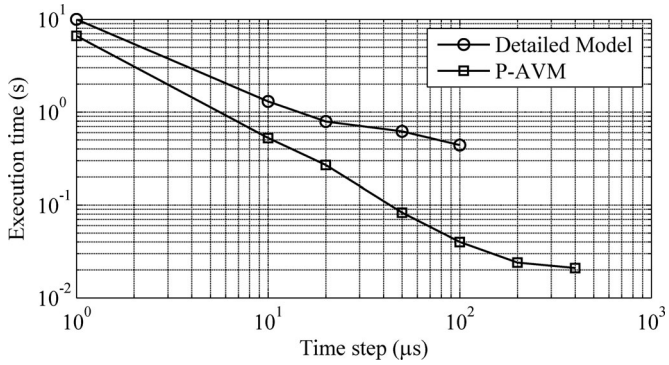

Fig. 15. Execution time versus time step.

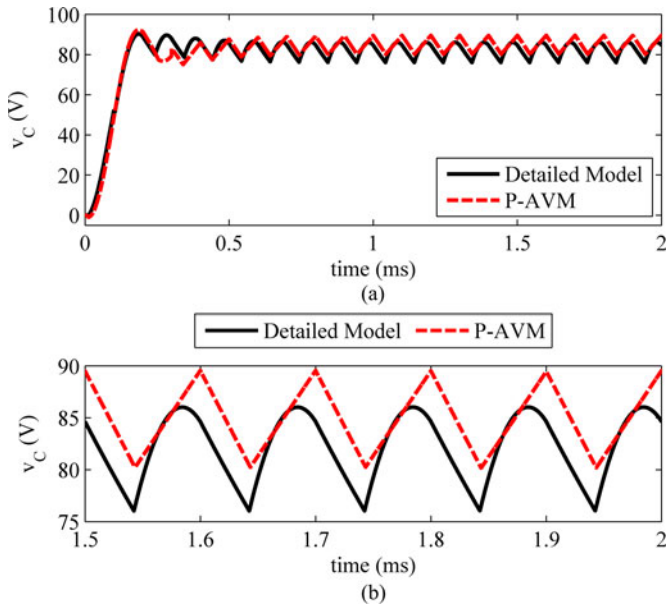

Fig. 16. Waveform of v_C during startup: (a) overall waveform and (b) zoomed in waveform. The switching frequency is 10 kHz.

events does not change with the time step. For the P-AVM, the iterative algorithm proposed in Section III-C is used to identify switching instants instead of handling individual switching events. The average number of iterations, i.e., $N_{i,\mathrm{ave}}$, is given in Table II. As the time step increases from 1 to 200 μs, $N_{i,\mathrm{ave}}$ varies within a small range, i.e., [1.229, 1.273]. As a result, the execution time is approximately inversely proportional to the time step, as shown in Fig. 15.

Assume that a maximum error less than 0.2 p.u. is acceptable. According to Table I, the detailed model and P-AVM can use a time step up to 50 and 100 μs, respectively. The corresponding

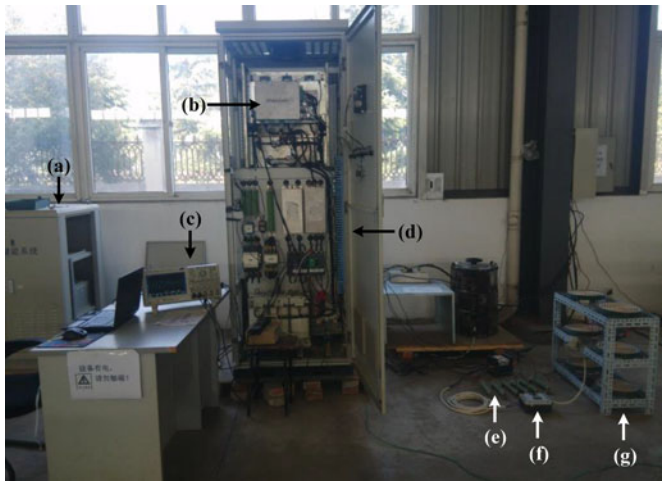

Fig. 17. Hardware setup: (a) lithium iron phosphate battery, (b) controller, (c) oscilloscope, (d) converter, filter, and transformer, (e) 100-Ω resistive load, (f) breaker, and (g) 40-Ω resistive load.

execution time for the detailed model and P-AVM is 0.62 and 0.04 s, respectively. The speed is improved by 15.5 times.

C. Discussions

In case of a low switching frequency or a small-value inductor or capacitor, the piecewise-linear ripple function, i.e., (37)–(39), may not represent real ripples very well. As a result, errors in switching instants will be induced and consequently the accuracy of the P-AVM will be reduced. As an example, set the switching frequency of the boost converter in Fig. 5 to 10 kHz. The linear state feedback controller, i.e., (45), is used to determine $V_{f,1}$. Simulate the startup transients using the detailed model and P-AVM, respectively. The waveform of v_C is shown in Fig. 16. The ripple in v_C is clearly not piecewise linear. An error in the average value of v_C is observed.

In this case, high-order switching-frequency-dependent AVMs, such as the TIMF AVM [36], can provide a better approximation to the ripples and improve the accuracy of simulation results. However, the computational burden will increase as well. Therefore, in order to choose proper models for specific applications, a tradeoff between accuracy and efficiency has to be made.

For a dc–dc converter, when the ripples in state variables are too large, the converter will turn to discontinuous conduction mode (DCM). In DCM, the transistor and diode as a group has three statuses: 1) the transistor conducts while the diode does not, 2) the diode conducts while the transistor does not, and 3) both the transistor and diode are off. Since the P-AVM and

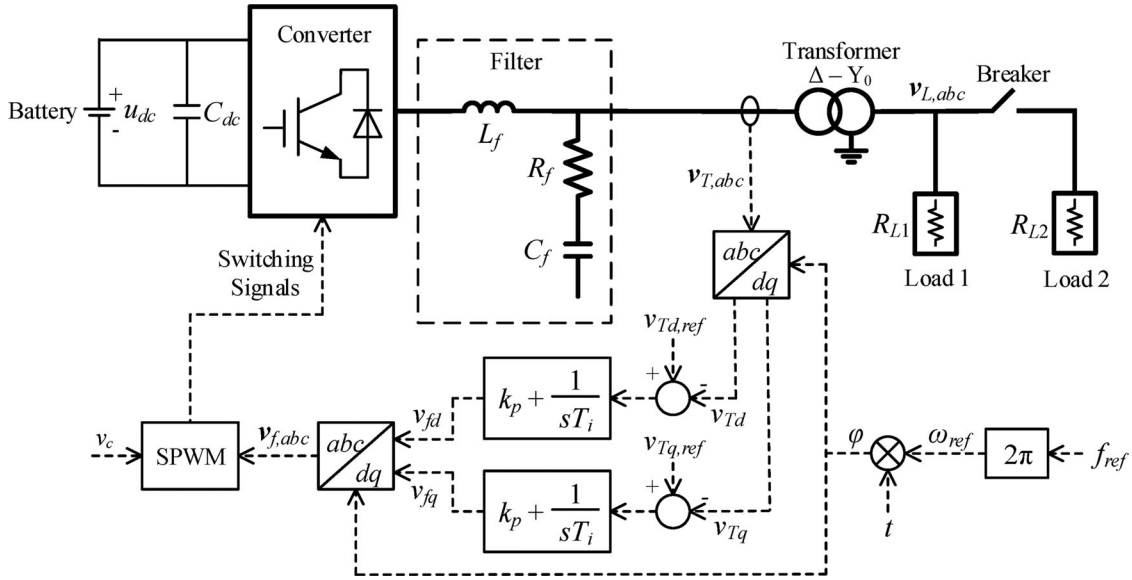

Fig. 18. Schematic of the experimental system.

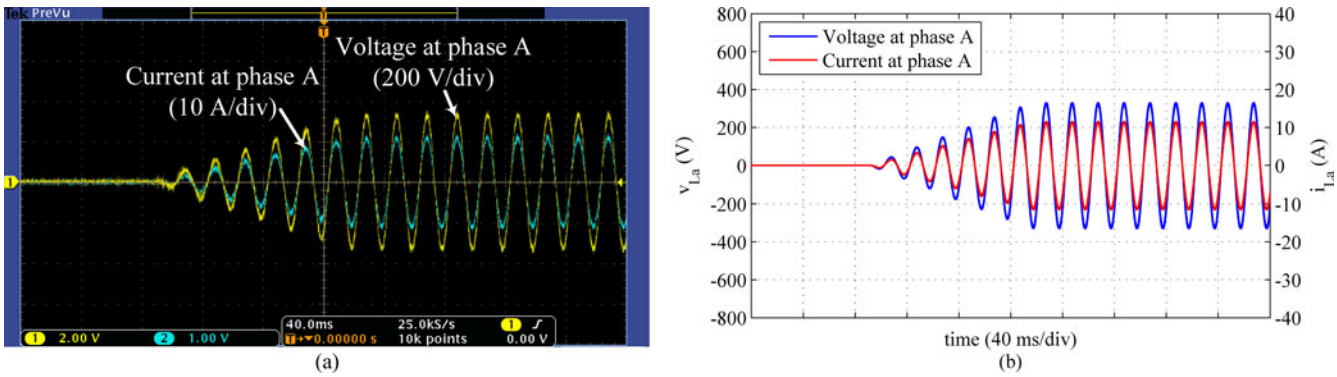

Fig. 19. Startup transients: (a) experimental results and (b) simulation results.

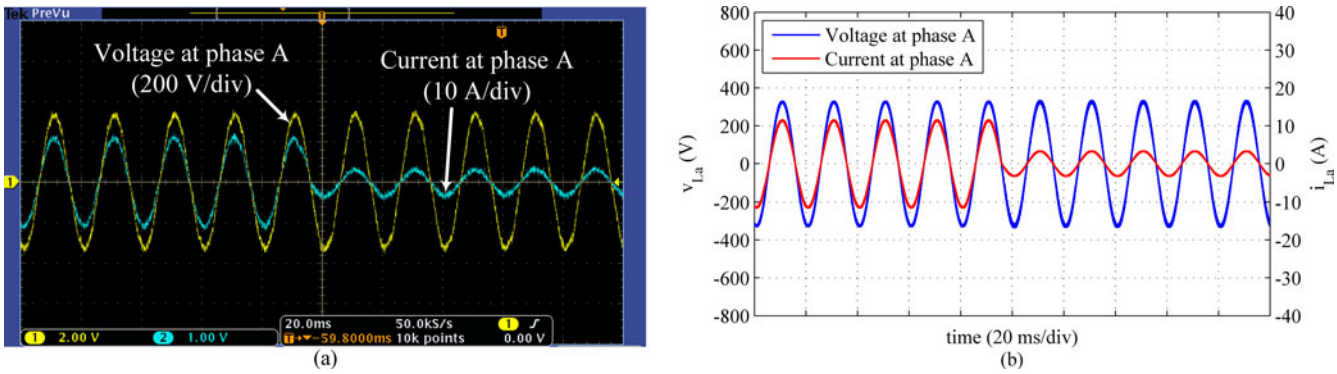

Fig. 20. Transient response to load change: (a) experimental results and (b) simulation results.

ripple function assume that a switch group has only two statuses and switching functions are binary-valued functions, they cannot be directly applied to converters operating in DCM.

This paper is focused on large-signal time-domain transient simulations. However, the P-AVM can also be applied to small-signal frequency-domain analysis. The small-signal characteristics of PWM converters are evaluated by a set of transfer functions, including the input-to-output transfer function, control-to-output transfer function, input impedance, and output impedance [12]. The transfer functions for open-loop converters can be extracted by linearization, as it is done for the T-AVM [48]. The only difference is that the P-AVM uses actual duty

ratios as control inputs while the T-AVM uses continuous duty ratios. For closed-loop converters, the actual duty ratio is determined by an iterative process, which cannot be formulated by an analytic transfer function. Therefore, the frequency sweep method [50] will be used to extract the closed-loop transfer functions from transient simulations.

V. Experimental Validation

A 50-kVA two-level three-phase ac–dc converter is used for experimental validation. The converter is a commercial product that can be applied to inverter-interfaced DERs, such as a photovoltaic array or a battery energy storage system. The hardware setup and schematic of the experimental system are shown in Figs. 17 and 18, respectively. The dc side of the converter is connected to a lithium iron phosphate battery that provides a stable dc voltage, while the ac side is connected to the load through a *RLC* filter and a transformer. Two resistive loads are connected in parallel with a breaker in between. A feedback control loop with a PI regulator is designed to maintain the magnitude of the load voltage, i.e., $\boldsymbol{v}_{L,abc}$. Instead of directly regulating $\boldsymbol{v}_{L,abc}$, the converter-side voltage of the transformer, i.e., $\boldsymbol{v}_{T,abc}$, is monitored and regulated. $\boldsymbol{v}_{T,abc}$ is converted to a rotating *dq*-reference frame whose rotational speed is determined by the reference of ac frequency, i.e., $f_{\rm ref}$. Therefore, the ac frequency is maintained at $f_{\rm ref}$ in the steady state. The parameters of the converter and controller are given in the Appendix.

A transient simulation model is developed for the experimental system based on the P-AVM and iterative algorithm proposed in this paper. With the two loads connected, the startup process is simulated and compared to the experimental results. To avoid large transients in startup and protect the converter, the reference of the transformer voltage at *d*-axis, i.e., $v_{Td,\rm ref}$, is ramped up with a constant rate from 0 to 0.203 kV in 0.125 s. The waveforms of the ac voltage and current at phase A, i.e., v_{La} and i_{La}, are shown in Fig. 19. In the steady state, the magnitude of v_{La} and i_{La} are 325 V and 11.4 A, respectively. Then the breaker is opened to disconnect Load 2 at a zero crossing point of i_{La}. The response of the converter is shown in Fig. 20. The magnitude of v_{La} and the ac frequency are maintained at their reference values by the controller. The magnitude of i_{La} is reduced to 3.25 A as a direct result of load disconnection. The simulation results match the experimental results in both scenarios.

VI. Conclusion

In this paper, a piecewise AVM with ripple estimation and an iterative algorithm are proposed for large-signal transient simulation of PWM converters. The simulation results indicate that the proposed model matches the detailed model under large ripple or large disturbance conditions. The results also show that only a small amount of additional computational effort is needed for iterations.

This paper also illustrates the limitations of traditional AVMs under large ripple and large disturbance conditions. The effect of feedback controllers on the performance of the traditional AVMs is discussed and demonstrated. The results are useful for understanding of the applicability of the traditional AVMs.

Limitations of the proposed method are discussed. In case of a low switching frequency or a small-value inductor or capacitor, the accuracy of piecewise AVM may reduce. The propose method cannot be applied to converters in DCM. Due to the need of iteration, it cannot be implemented in commercial simulation tools, such as PSCAD/EMTDC, which do not support iteration over multiple time steps. Further study is needed to eliminate iteration and design an interface to integrate the piecewise AVM and ripple function into commonly used simulation tools.

Appendix

Parameters of the boost converter (see Section IV-A) are

$E = 48\,\text{V}$, $L = 100\,\mu\text{H}$, $C = 33\,\mu\text{F}$, $R = 12\,\Omega$, $V_1 = 0.25\,\text{V}$, $k_1 = 0.02$, $k_2 = -0.008$, $V_2 = 5\,\text{V}$, $H = 1/24$, $K_p = 0.001$, $T_i = 0.01\,\text{s}$.

Parameters of the two-level three-phase ac–dc converter (see Section IV-B) are

$f = 50\,\text{Hz}$, $\omega = 2\pi f$, $u_a = 326.6\sin(\omega t)\ \text{V}$, $u_b = 326.6\sin(\omega t - 120^\circ)\ \text{V}$, $u_c = 326.6\sin(\omega t + 120^\circ)\ \text{V}$, $R_f = 0.001\,\Omega$, $L_f = 0.6\,\text{mH}$, $C_{dc} = 16\,\text{mF}$, $R_L = 2\,\Omega$, $S_{\rm base} = 1\,\text{MW}$, $V_{\rm base} = 326.6\,\text{V}$, $u_{\rm dc,ref} = 3.6742\,\text{p.u.}$, $i_{q,\rm ref} = 0\,\text{p.u.}$, $k_{p1} = 1$, $T_{i1} = 0.1\,\text{s}$, $k_{p2} = 6$, $T_{i2} = 0.01\,\text{s}$.

Parameters of the experimental system (see Section V) are

Rated kVA of converter = 50 kVA, switching frequency $f_s = 6.4\,\text{kHz}$, rated voltages of transformer = 0.25/0.4 kV, $u_{\rm dc} = 0.58\,\text{kV}$, $C_{\rm dc} = 6000\,\mu\text{F}$, $L_f = 0.4\,\text{mH}$, $R_f = 0.2\,\Omega$, $C_f = 30\,\mu\text{F}$, $R_{L1} = 100\,\Omega$, $R_{L2} = 40\,\Omega$, $v_{Td,\rm ref} = 0.203\,\text{kV}$, $v_{Tq,\rm ref} = 0\,\text{kV}$, $f_{\rm ref} = 50\,\text{Hz}$, $k_p = 1$, $T_i = 0.001\,\text{s}$.

References

[1] J. Brochu, C. Larose, and R. Gagnon, "Validation of single- and multiple-machine equivalents for modeling wind power plants," *IEEE Trans. Energy Convers.*, vol. 26, no. 2, pp. 532–541, Jun. 2011.

[2] M. O. Faruque, V. Dinavahi, S. Santoso, and R. Adapa, "Review of electromagnetic transient models for non-VSC FACTS," *IEEE Trans. Power Del.*, vol. 20, no. 2, pp. 1065–1079, Apr. 2005.

[3] M. Saeedifard and R. Iravani, "Dynamic performance of a modular multilevel back-to-back HVDC system," *IEEE Trans. Power Del.*, vol. 25, no. 4, pp. 2903–2912, Oct. 2010.

[4] A. H. Etemadi and R. Iravani, "Overcurrent and overload protection of directly voltage-controlled distributed resources in a microgrid," *IEEE Tran. Ind. Electron.*, vol. 60, no. 12, pp. 5629–5638, Dec. 2013.

[5] A. Khaligh and Z. Li, "Battery, ultracapacitor, fuel cell, and hybrid energy storage systems for electric, hybrid electric fuel cell, and plug-in hybrid electric vehicles: State of the art," *IEEE Trans. Veh. Technol.*, vol. 59, no. 6, pp. 2806–2814, Jul. 2010.

[6] N. Watson and J. Arrillaga, *Power Systems Electromagnetic Transients Simulation*. London, U.K.: Inst. Eng. Technol., 2007.

[7] D. Maksimovic, A. M. Stankovic, V. J. Thottuvelil, and G. C. Verghese, "Modeling and simulation of power electronic converters," *Proc. IEEE*, vol. 89, no. 6, pp. 898–912, Jun. 2001.

[8] PSCAD/EMTDC Simulation Tool. Manitoba HVDC Research Center, (2014). [Online]. Available: https://hvdc.ca/pscad/

[9] MATLAB/Simulink Simulation Tool. MathWorks, Inc. (2014). [Online]. Available: http://www.mathworks.com

[10] M. O. Faruque, V. Dinavahi, and W. Xu, "Algorithm for the accounting of multiple switching events in digital simulation of power-electronic systems," *IEEE Trans. Power Del.*, vol. 20, no. 2, pp. 1157–1167, Apr. 2005.

[11] J. R. Marti and J. Lin, "Suppression of numerical oscillations in the EMTP," *IEEE Trans. Power Syst.*, vol. 4, no. 2, pp. 739–747, May 1989.

[12] S. Chiniforoosh, J. Jatskevich, A. Yazdani, V. Sood, V. Dinavahi, J. A. Martinez, and A. Ramirez, "Definitions and applications of dynamic average models for analysis of power systems," *IEEE Trans. Power Del.*, vol. 25, no. 4, pp. 2655–2669, Oct. 2010.

[13] E. Tara, S. Filizadeh, J. Jatskevich, E. Dirks, A. Davoudi, M. Saeedifard, K. Strunz, and V. K. Sood, "Dynamic average-value modeling of hybrid-electric vehicular power systems," *IEEE Trans. Power Del.*, vol. 27, no. 1, pp. 430–438, Jan. 2012.
[14] S. Chiniforoosh, H. Atighechi, A. Davoudi, J. Jatskevich, J. A. Martinez, M. Saeedifard, D. C. Aliprantis, and V. K. Sood, "Steady-state and dynamic performance of front-end diode rectifier loads as predicted by dynamic average-value models," *IEEE Trans. Power Del.*, vol. 28, no. 3, pp. 1533–1541, Jul. 2013.
[15] S. Chiniforoosh, H. Atighechi, A. Davoudi, J. Jatskevich, A. Yazdani, S. Filizadeh, M. Saeedifard, J. A. Martinez, V. Sood, K. Strunz, J. Mahseredjian, and V. Dinavahi, "Dynamic average modeling of front-end diode rectifier loads considering discontinuous condition mode and unbalanced operation," *IEEE Trans. Power Del.*, vol. 27, no. 1, pp. 421–429, Jan. 2012.
[16] J. A. Sanders, F. Verhulst, and J. Murdock, *Averaging Methods in Nonlinear Dynamical Systems*. New York, NY, USA: Springer, 2007.
[17] R. Tymerski and V. Vorperian, "Generation, classification and analysis of switched-mode dc-to-dc converters by the use of switched-inductor cells," in *Proc. IEEE Int. Telecommun. Energy Conf.*, Oct. 1986, pp. 181–195.
[18] E. van Dijk, H. J. N. Spruijt, D. M. O'Sullivan, and J. B. Klaassens, "PWM-switch modeling of dc-dc converters," *IEEE Trans. Power Electron.*, vol. 10, no. 6, pp. 659–665, Nov. 1995.
[19] S. R. Sanders and G. C. Verghese, "Synthesis of averaged circuit models for switched power converters," *IEEE Trans. Circuit Syst.*, vol. 38, no. 8, pp. 905–915, Aug. 1991.
[20] R. D. Middlebrook, "Small-signal modeling of pulse-width modulated switched-mode power converters," *Proc. IEEE*, vol. 76, no. 4, pp. 343–354, Apr. 1988.
[21] Y. Amran, F. Huliehel, and S. Ben-Yaakov, "A unified SPICE compatible average model of PWM converters," *IEEE Trans. Power Electron.*, vol. 6, no. 4, pp. 585–594, Oct. 1991.
[22] S. Ben-Yaakov, "Average simulation of PWM converters by direct implementation of behavioral relationships," in *Proc. 8th Annu. IEEE Applied Power Electron. Conf. Expo.*, Mar. 1993, pp. 510–516.
[23] P. T. Krein, J. Bentsman, R. M. Bass, and B. L. Lesieutre, "On the use of averaging for the analysis of power electronic system," *IEEE Trans. Power Electron.*, vol. 5, no. 2, pp. 182–190, Apr. 1990.
[24] J. Sun, D. M. Mitchell, M. F. Greuel, P. T. Krein, and R. M. Bass, "Averaged modeling of PWM coverters operating in discontinuous conduction mode," *IEEE Trans. Power Electron.*, vol. 16, no. 4, pp. 482–492, Jul. 2001.
[25] J. Jatskevich, S. D. Pekarek, and A. Davoudi, "Parametric average-value model of synchronous machine-rectifier systems," *IEEE Trans. Energy Convers.*, vol. 21, no. 1, pp. 9–18, Mar. 2006.
[26] A. Dubey, S. Santoso, and M. P. Cloud, "Average-value model of electric vehicle chargers," *IEEE Trans. Smart Grid*, vol. 4, no. 3, pp. 1549–1557, Sep. 2013.
[27] J. Sun, "Symbolic analysis methods for averaged modeling of switching power converters," *IEEE Trans. Power Electron.*, vol. 12, no. 3, pp. 537–546, May 1997.
[28] S. R. Sanders, J. M. Noworolski, X. Z. Liu, and G. C. Verghese, "Generalized averaging method for power conversion circuits," *IEEE Trans. Power Electron.*, vol. 6, no. 2, pp. 251–259, Apr. 1991.
[29] M. Daryabak, S. Filizadeh, J. Jatskevich, A. Davoudi, M. Saeedifard, V. K. Sood, J. A. Martinez, D. Aliprantis, J. Cano, and A. Mehrizi-Sani, "Modeling of LCC-HVDC systems using dynamic phasors," *IEEE Trans. Power Del.*, vol. 29, no. 4, pp. 1989–1998, Aug. 2014.
[30] J. Mahdavi, A. Emaadi, M. D. Bellar, and M. Ehsani, "Analysis of power electronic converters using the generalized state-space averaging approach," *IEEE Trans. Circuits Syst. I, Fundam. Theory Appl.*, vol. 44, no. 8, pp. 767–770, Aug. 1997.
[31] Y. Fuad, W. L. de Koning, and J. W. van der Woude, "On the stability of the pulsewidth-modulated Cuk converter," *IEEE Trans. Circuits Syst. II, Exp. Briefs*, vol. 51, no. 8, pp. 412–420, Aug. 2004.
[32] A. Yazdani and R. Iravani, "A generalized state-space averaged model of the three-level NPC converter for systematic dc-voltage balancer and current-controller design," *IEEE Trans. Power Del.*, vol. 20, no. 2, pp. 1105–1114, Apr. 2005.
[33] B. Lehman and R. M. Bass, "Extensions of averaging theory for power electronic systems," *IEEE Trans. Power Electron.*, vol. 11, no. 4, pp. 542–553, Jul. 1996.
[34] J. W. Kimball and P. T. Krein, "Singular perturbation theory for dc-dc converters and application to PFC converters," *IEEE Trans. Power Electron.*, vol. 23, no. 6, pp. 2970–2981, Nov. 2008.
[35] J. Sun, "Characterization and performance comparison of ripple-based control for voltage regulator modules," *IEEE Trans. Power Electron.*, vol. 21, no. 2, pp. 346–353, Mar. 2006.
[36] H. Behjati, L. Niu, A. Davoudi, and P. L. Chapman, "Alternative time-invariant multi-frequency modeling of PWM dc-dc converters," *IEEE Trans. Circuits Syst. I, Reg. Papers*, vol. 60, no. 11, pp. 3069–3079, Nov. 2013.
[37] A. Davoudi and J. Jatskevich, "Parasitics realization in state-space average-value modeling of PWM dc-dc converters using an equal area method," *IEEE Trans. Circuits Syst. I, Reg. Papers*, vol. 54, no. 9, pp. 1960–1967, Sep. 2007.
[38] A. Davoudi, J. Jatskevich, and T. De Rybel, "Numerical state-space average-value modeling of PWM dc-dc converters operating in DCM and CCM," *IEEE Trans. Power Electron.*, vol. 21, no. 4, pp. 1003–1012, Jul. 2006.
[39] A. Davoudi, J. Jatskevich, and P. L. Chapman, "Computer-aided dynamic characterization of fourth-order PWM dc-dc converters," *IEEE Trans. Circuits Syst. II, Exp. Briefs*, vol. 55, no. 10, pp. 1021–1025, Oct. 2008.
[40] A. Davoudi, J. Jatskevich, and P. L. Chapman, "Numerical dynamic characterization of peak current-mode-controlled dc-dc converters," *IEEE Trans. Circuits Syst. II, Exp. Briefs*, vol. 56, no. 12, pp. 906–910, Dec. 2009.
[41] I. Zafrany and S. Ben-Yaakov, "Generalized switched inductor model (GSIM): Accounting for conduction losses," *IEEE Trans. Aerosp. Electron. Syst.*, vol. 38, no. 2, pp. 681–687, Apr. 2002.
[42] Y. Xu, Y. Chen, L. Chen, and S. Mei, "Integrating an improved averaged model for PWM converters into EMTP," *IEEE Trans. Power Del.*, vol. 29, no. 1, pp. 291–293, Feb. 2014.
[43] B. Lehman and R. M. Bass, "Switching frequency dependent averaged models for PWM dc-dc converters," *IEEE Trans. Power Electron.*, vol. 11, no. 1, pp. 89–98, Jan. 1996.
[44] T. A. Sakharuk, B. Lehman, A. M. Stankovic, and G. Tadmor, "Effects of finite switching frequency and delay on PWM controlled systems," *IEEE Trans. Circuits Syst. I, Fundam. Theory Appl.*, vol. 47, no. 4, pp. 555–567, Apr. 2000.
[45] Z. Mihajlovic, B. Lehman, and C. Sun, "Output ripple analysis of switching dc-dc converters," *IEEE Trans. Circuits Syst. I, Reg. Papers*, vol. 51, no. 8, pp. 1596–1611, Aug. 2004.
[46] A. Abramovitz, "An approach to average modeling and simulation of switch-mode systems," *IEEE Trans. Educ.*, vol. 54, no. 3, pp. 509–517, Aug. 2011.
[47] P. C. Krause, O. Wasynczuk, S. D. Sudhoff, and S. Pekarek, *Analysis of Electric Machinery and Drive System*. Hoboken, NJ, USA: Wiley, 2013.
[48] R. W. Erickson and D. Maksimovic, *Fundamentals of Power Electronics*. New York, NY, USA: Kluwer, 2004.
[49] G. E. Dullerud and F. Paganini, *A Course in Robust Control Theory: A Convex Approach*. New York, NY, USA: Springer, 2000.
[50] M. B. Harris, A. W. Kelley, J. P. Rhode, and M. E. Baran, "Instrumentation for measurement of line impedance," in *Proc. IEEE Appl. Power Electron. Conf.*, Feb. 1994, pp. 887–893.

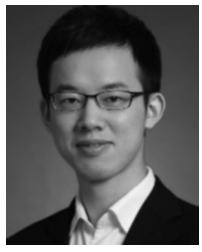

Yin Xu (S'12–M'14) received the B.E. and Ph.D. degrees in electrical engineering from Tsinghua University, Beijing, China, in 2008 and 2013, respectively.

He is currently an Assistant Research Professor at the School of Electrical Engineering and Computer Science, Washington State University, Pullman, WA, USA. His research interests include power system modeling and simulation, distribution system resiliency, service restoration, distribution automation, and microgrids.

Ying Chen (M'07) received the B.E. and Ph.D. degrees from Tsinghua University, Beijing, China, in 2001 and 2006, respectively, both in electrical engineering.

He is currently an Associate Professor at the Department of Electrical Engineering, Tsinghua University. His research interests are in the areas of power system dynamics and simulation, parallel computing, and grid computing.

Chen-Ching Liu (S'80–M'83–SM'90–F'94) received the Ph.D. degree from the University of California, Berkeley, CA, USA, in 1983.

He served as a Professor at the University of Washington, Seattle, WA, USA, from 1983–2005. During 2006–2008, he was the Palmer Chair Professor at Iowa State University, Ames, IA, USA. During 2008–2011, he was a Professor and Acting/Deputy Principal of the College of Engineering, Mathematical and Physical Sciences, University College Dublin, Dublin, Ireland. He is currently the Boeing Distinguished Professor of electrical engineering and the Director of the Energy Systems Innovation Center, Washington State University, Pullman, WA.

Dr. Liu received the IEEE PES Outstanding Power Engineering Educator Award in 2004. In 2013, he received the *Doctor Honoris Causa* from the Polytechnic University of Bucharest, Bucharest, Romania. He served as the Chair of the IEEE PES Technical Committee on Power System Analysis, Computing, and Economics during 2005–2006.

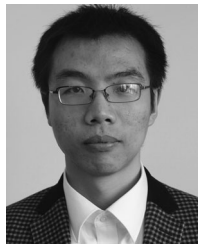

Haixiang Gao (S'12) received the B.E. degree in electrical engineering from Tsinghua University, Beijing, China, in 2011, where he is working toward the Ph.D. degree.

His research interests include electromagnetic transient simulation and parallel computing for power systems.